UNIVERSITY OF THE WITWATERSRAND

School of Physics

A dissertation submitted to the School of Physics, Faculty of Science, University of the Witwatersrand in fulfilment of the academic requirements of the degree of Master of Science.

PROBING DARK MATTER IN THE MADALA HYPOTHESIS USING MEERKAT

Author:
Ralekete Khilly Temo

Supervisor:
Dr. Geoff Beck

Johannesburg, June 11, 2022

Abstract

The Madala hypothesis was introduced to explain several anomalies observed at the Large Hadron Collider. This model introduces a dark matter candidate χ through the extension of the standard model's Higgs-sector, i.e. an extra Higgs doublet (2HDM) and an additional scalar boson S are introduced, which can couple to dark matter. Assuming the Madala hypothesis can explain the cosmic ray spectra and the Milky Way galactic centre's gamma-ray flux excesses observed by AMS-02 and Fermi-LAT experiments, respectively. The aim of this dissertation is to compute the allowed parameter space for the 2HDM+S model, subsequently, make synchrotron emission predictions for observations with MeerKAT and other radio telescopes. The regions of interest for the predictions are the Reticulum II, Coma cluster, Ophiuchus cluster and M31 (Andromeda galaxy). However, only Reticulum II dwarf galaxy is considered for MeerKAT predictions, while for the remaining three objects, the constraints on the parameter space that can be derived from available radio observations are derived. The MeerKAT predictions and radio observation exclusion limits will collectively instigate the validation of our assumption and allow us to constrain the particle properties of the Madala hypothesis from an astrophysical standpoint while showcasing the power of MeerKAT in indirect dark matter searches.

Declaration of Authorship

The work described by this thesis was carried out at the University of the Witwatersrand, Department of Physics, from February 2020 until June 2022, under the supervision of Doctor Geoff Beck.
This thesis is entirely, unless specifically contradicted in the text, the work of the candidate, Ralekete Khilly Temo, and has not been previously submitted, in whole or in part, to any other tertiary institution. Where use has been made of the work of others, it is duly acknowledged in the text.

Signed:

Date:
11 June 2022

Declaration - Plagiarism

I, Ralekete Khilly Temo declare that,

- The research reported in this thesis, except where otherwise indicated, is my original research.
- This thesis has not been submitted for any degree or examination at any other university.
- This thesis does not contain other persons' data, pictures, graphs or other information, unless specifically acknowledged as being sourced from other persons.
- This thesis does not contain other persons' writing, unless specifically acknowledged as being sourced from other researchers. Where other written sources have been quoted, then:
  a. Their words have been rewritten but the general information attributed to them has been referenced.
  b. Where their exact words have been used, then their writing has been placed in italics and inside quotation marks, and referenced.
- This thesis does not contain, text, graphics or tables copied and pasted from the Internet, unless specifically acknowledged, and the source being detailed in the thesis and in the References sections.

Signed:

Declaration - Publications

Details of publications that form part and/or include research presented in this thesis. The candidate undersigned declares that following data is correct and accurate. Additionally, the candidate certifies that his contributions, as detailed here and in the introduction to each mentioned chapter, are accurate and true.
Signed:

1. **Title:** Connecting multi-lepton anomalies at the LHC and in Astrophysics with MeerKAT/SKA

   Status: Preprint submitted to Physics of the Dark Universe. ArXiV pre-print available [1].

   Authors: G. Beck, R. Temo, E. Malwa, M. Kumar and B. Mellado

   Contributions: Wrote a python code that produced the parameter spaces in Figure 2 of the paper. Composed some of the text for sections 3 (particularly the propagation of positrons) and 4 (the prominence of the radio-band indirect dark matter search) of the paper.

2. **Title:** Probing dark matter in the Madala model using radio observations

   Status: Accepted by SAIP for publication.

   Authors: R. Temo and G. Beck

   Contributions: Produced the text, results and discussions presented in the paper.

Acknowledgements

Firstly, I would like to acknowledge and express my sincere gratitude to my supervisor Dr. Geoff Beck for his perpetual support, constructive guidance, and for helping me settle some of my school fees in the 2021 academic year. I have gained a lot of knowledge from him, it was an honor to learn from such a bright mind and he continues to be a role model to me. I acknowledge Prof. Andrew Chen and Prof. Bruce Mellado for granting me a bursary for the 2020 academic year. Crafting the programming skills needed for my project would not have been possible if it was not for my friend Unathi Skosana, who suggested materials and guidance to get me started with programming.

Of course, this thesis was not going to be if it was not for the support of people outside my academic career, I will just mention their names because if I were to mention their contributions, I undoubtedly need another thesis for that. To Lebo, Lunga, Motlalepula, Apigail, Bubsie, Buda, Thapelo, Tiisetso, Davido, Muele, Pollen, Musa, Phenyo, and Nathi, thank you for supporting and keeping me sane through this journey.

It would be a crime to not acknowledge my family especially my sisters (Nono, Pensive, Nolyn, and Given) and father, thank you for the unconditional support and for always believing in me, I am deeply blessed to have you all in my life.

Last but not least, I would like to acknowledge the South African Research Chairs Initiative of the Department of Science and Technology and National Research Foundation of South Africa for the financial support [1].

[1] Opinions expressed and conclusions arrived at, are those of the author and are not necessarily to be attributed to the NRF.

Dedicated to my late mom, Masenyakane Daphney "My Ma" Temo, 1963 July 04 - 2017 September 23

Contents

List of Figures

List of Tables

Chapter 1

Introduction

Observational evidence suggests that roughly 85% of the mass of the universe eventuates from the contribution of a rather mysterious and non-baryonic matter component, famously known as dark matter (DM) [2–4]. DM is one of the unsolved puzzles that has been vexing the modern physics and astronomy community, and its existence has some imperative implications. The existence of DM is supported immensely by astrophysical and cosmological evidence, this includes rotational curves of galaxies [5], motion of galaxies in galaxy clusters [6], gravitational lensing [7, 8], Cosmic Microwave Background (CMB) anisotropy data [9–11], and light-element abundance predictions emanating from big-bang nucleosynthesis [12, 13]. However, laboratory experiments on Earth are yet to detect direct signatures of DM and its particle nature is still unknown. This lead to the development of a multitude of theoretical models to explain the particle nature of DM. One such a model is the Madala hypothesis, which was proposed to explain several anomalies seen from the Large Hadron Collider (LHC) data in both CMS and ATLAS experiments [14–18]. This hypothesis provides a DM candidate through the extension of the standard model (SM) by introducing heavier scalar bosons. The study of the possible astrophysical consequences of the DM candidate provided by the Madala hypothesis can be pivotal in constraining the particle properties in this model (see e.g [19–21]).
In the regime of astrophysical observations, cosmic-ray (positrons and antiprotons) excesses are observed by the Alpha Magnetic Spectrometer (AMS-02) [22,23], and excesses are seen by Fermi-LAT [24] in gamma-ray fluxes from the Milky-Way's galactic centre. In this work, we employ the Madala hypothesis to describe the aforementioned excesses. The approach is to compute the allowed parameter space within systematic uncertainties. The allowed parameter spaces will help gauge whether the produced yield functions per DM annihilation for the Madala hypothesis are consistent with astrophysical

observations or not. In this dissertation, the goal is to constrain the allowed parameter space in terms of the DM mass and the thermal cross-section. Thereafter, the allowed parameter space will be used to make synchrotron emission predictions. The sources of interest for this work are Reticulum II, Coma Cluster, M31, and Ophiuchus cluster. Given we have a constrained model, our Reticulum II predictions can be tested independently via radio observation with the MeerKAT telescope. Furthermore, we derive constraints on the allowed parameter space using the available radio observation data for M31 as well as Coma and Ophiuchus galaxy clusters.

In the introduction chapter, we will give a brief introduction pertaining to the DM problem, this includes the observational evidence in favour of the existence of the non-baryonic DM, an overview of the particle solution to the DM problem, thermal history of DM, density distributions that characterise DM and an overview of detection modes of DM, as well as the relevance of MeerKAT in indirect DM search.

1.1 Observational Evidence of Dark Matter

In 1933, Fritz Zwicky suggested that to obtain the observed orbital velocities of galaxies for the Coma Cluster, the average density of the cluster has to be 400 times larger than the luminous matter density of the cluster. Hence, suggesting the existence of matter which is “dark” [6].

1.1.1 Rotation Curves of Galaxies

A more sophisticated approach came in 1970, Rubin and Ford made an astounding discovery that the rotation curves of galaxies are flat [5]. This means that the orbital velocity of the stellar objects within galaxies, as a function of radial distance from the galactic center, remained constant up to larger radii. This was a huge controversy since a radial decline was expected, following Keplerian predictions from the visible matter [25]. As a consequence of the discovery, observations were extended to other galaxies, including our Milky Way, and this revealed that they are also characterised by almost flat rotation curves [26]. The presence of the stellar objects that constitute the galaxy alone can not account for the behavior and nature of the rotation curves, this is where the presence of dark matter comes to the rescue since it provides a gravitational force that keeps the orbital velocity of objects constant, and models with dark matter explain these flat rotation curves and also yield arguably good fits to data [25]. But the rotation curves measurement is subject to limitations, this includes the fact that their observation can only be executed as far as there are stars and/or concentration of neutral hydrogen, and that is roughly about a distance of tens of kpc [25].

1.1.2 Gravitational Lensing

The investigation of the distribution of dark matter can be executed most directly through the gravitational effects on baryonic matter [27]. Einstein's theory of general relativity suggests that the curvature of space-time near any gravitating mass bends/deflects passing light rays, and thus what an observer sees is a shifted, distorted, and magnified images of the background source [28–30]. The aforementioned phenomenon is called gravitational lensing, and it is analogous to optical refraction, the distinction is that different physics are involved. Gravitational lensing has been used as a tool to infer the mass distribution of galaxy clusters, where the large mass associated with the cluster makes it easier for the gravitationally induced ellipticity of background galaxies to be detected [27]. Through the use of gravitational lensing, Sloan Digital Sky Survey (SDSS) was able to elucidate that most galaxies, including the Milky Way, consist of more mass than initially speculated and the majority of the mass is accounted for by dark matter [31]. This technique, even though it addresses the limitations that afflict rotation curve measurements, is also characterised by inherent uncertainties. However, it provides rigorous evidence for the dominance of dark matter in galaxies and galaxy clusters [32].

1.1.3 CMB Observations

Another prominent evidence for dark matter comes from the extensive studies of the cosmic microwave background. Modern observations such as the Cosmic Background Explorer (COBE), Wilkinson Microwave Anisotropy Probe (WMAP), and the Planck mission found the relative magnitude of CMB anisotropies to be about 10^{-5} [33, 34], this dictates the amplitude of primordial density fluctuations that become the cosmic structure as a consequence of amplification by gravity. Furthermore, the observed CMB anisotropies at a level of 10^{-5} would not have been sufficient to produce the present cosmic structure if matter has detached from radiation at the recombination epoch. Hence, there is a necessity for an additional (and dominant) matter not coupled with radiation at the recombination epoch (i.e. a non-baryonic matter). The data from the aforementioned experiments suggest that, for the perturbations to produce all the non-linear structure presently observed, the value of the matter density parameter must be roughly $\Omega_m \sim 0.3$, where $\Omega_m = \frac{\rho_m}{\rho_c}$, ρ_m is the matter density, ρ_c is the critical density of the universe [35]. This argument further gains strength from the second acoustic peak of the CMB power spectrum, which from the amplitude of the peak yields a baryonic density fraction of roughly $\Omega_b \sim 0.05$, insinuating that the major contribution of the matter density parameter is from the non-baryonic dark matter [35].

1.1.4 Big-Bang Nucleosynthesis

Another evidence in favour of the existence of non-baryonic dark matter comes from the comparison between the theoretical predictions and observations of big-bang nucleosynthesis-induced light-elements abundance, which allows to place tighter constraints on the density parameter of baryons, i.e. $\Omega_b \sim 0.05$ [36–38]. The aforementioned can intuitively be delineated by considering that the big-bang nucleosynthesis is sensitive to the baryon-to-photon ratio $\eta \equiv \frac{n_b}{\eta_\gamma} \sim 10^{-9}$ [39]. But the density parameter of baryons is given by,

$$\Omega_b \equiv \frac{\rho_b}{\rho_c}. \tag{1.1}$$

The density of baryons in terms of baryon-to-photon ratio is given by $\rho_b = n_b m_p = \eta\eta_\gamma m_p$ and the critical density ρ_c today is taken as 1.9×10^{-29} h^2 g cm^{-3} [39] [1], where m_p denotes the mass of a proton, and η_γ (410.5 cm^{-3}) denotes the photon density as measured by the CMB temperature in present time. Then Eq. (1.1) becomes,

$$\Omega_b \equiv \frac{\eta\eta_\gamma m_p}{\rho_c} \sim 0.05. \tag{1.2}$$

1.2 Proposed Solutions to the Dark Matter Problem

In the previous section, the evidence for the existence of dark matter only tells us the location and amount of dark matter in the universe. However, the nature of dark matter remains elusive. The traditionally proposed solution is that dark matter is constituted by some particle, which is yet to be discovered. Arguably this gives rise to a wealth of possible candidates, hence a categorization scheme needs to be established to aid how the search for the candidate should be conducted. In the non-baryonic regime, the common categorization scheme is the one of subdividing particles according to their average velocity, where DM models with ultra-relativistic particles at decoupling are referred to as “hot”, while ones with non-relativistic particles are

[1]Here we assume $h \approx 0.7$.

referred to as "cold" [35,40]. The division has some imperative consequences for the formation of cosmic structure, where the extensive studies of the formation of galaxies can give a hint of whether dark matter is cold or hot [40]. Cosmological simulations of hot DM indicate that such models are unviable as dominant components of DM, since they fail to reproduce the cosmic structure observed presently [40,41]. In this work, we will focus mainly on a category of cold dark matter particle, the Weakly Interacting Massive Particles (WIMPs), which manifest from various extensions of the standard model. The reason why the WIMP has been a persistent and favourite candidate, is because it can naturally account for its cosmological abundance through the thermal "freeze-out" (see Section 1.3). WIMPs are characterised by several properties determining whether we can detect dark matter experimentally. The properties include mass, lifetime, scattering cross-section with nucleons, annihilation cross-section, and lastly the products which the WIMPs decay/annihilate into. Traditionally in the WIMPs DM model, the WIMPs are essentially in thermal and chemical equilibrium with rest of the particles in the early universe, and this is simply achieved through self-annihilation into SM particles and vice versa. But as the universe expands, the temperature of the universe drops below the mass of WIMPs and they can no longer be produced by interactions within the equilibrium state, thus they freeze-out from equilibrium, resulting in the comoving number density of WIMPs remaining the same. The self-annihilation cross-section is limited to the value of $\langle \sigma v \rangle \sim 3 \times 10^{-26}$ cm^3 s^{-1}, in order to induce the appropriate relic density [42]. More concrete discussion regarding the thermal history of DM will be given in the next section (Section 1.3).

1.3 Thermal History of Dark Matter

In this section, we will use units in which the Boltzmann's constant and speed of light are set to unity, i.e. $k_B = c = 1$, so that the temperature has units of energy. To understand the thermal history of a stable DM particle (e. g. WIMPs) χ with mass M_χ, the pivotal quantity to probe is the interaction rate,

$$\Gamma = n\sigma v, \tag{1.3}$$

where n is the number density of DM particles, σ is the cross-section of the interactions, and v is the average velocity of the particles. As long as $\Gamma \gg H$[2], local thermal equilibrium will be maintained at the temperature T of the universe. Thermal equilibrium is maintained by the stable DM particle

[2] $H = \frac{\dot{a}}{a}$ is known as the Hubble constant and gives the rate of expansion of the universe. Where a denotes the scale factor of the universe for the Friedmann-Robertson-Walker

χ annihilating with its anti-particle $\overline{\chi}$ producing lighter standard model (SM) particle l and its anti-particle $\bar{l}$, and vice versa,

$$\chi + \overline{\chi} \leftrightarrow l + \bar{l}. \tag{1.4}$$

As the universe expands the temperature of the universe drops, subsequently Γ also drops. When $T \ll M_\chi$ the DM particles become non-relativistic and their number density becomes Boltzmann suppressed ($n_\chi \propto e^{-M_\chi/T}$). As a consequence, the thermal equilibrium can no longer be maintained. At this stage, the annihilation process halts and the DM particles freeze-out[3] from equilibrium, then a relic density cosmological abundance remains.
The time evolution of the number density n_χ of DM particle χ is described by the Boltzmann equation [43–45],

$$\frac{dn_\chi}{dt} + 3\frac{\dot{a}}{a}n_\chi = -\langle\sigma v\rangle[n_\chi^2 - (n_\chi^{eq})^2], \tag{1.5}$$

where n_χ^{eq} denotes the number density of DM in thermal equilibrium and $\langle\sigma V\rangle$ denotes the thermally velocity-averaged DM annihilation cross section. The second term of the left-hand side of Eq. (1.5) can be absorbed by rewriting the equation as,

$$\frac{1}{a^3}\frac{d(n_\chi a^3)}{dt} = -\langle\sigma v\rangle[n_\chi^2 - (n_\chi^{eq})^2]. \tag{1.6}$$

A pivotal quantity to introduce when solely considering the study of the DM cosmological density is Y_χ, which is defined by,

$$Y_\chi = \frac{n_\chi}{s}, \tag{1.7}$$

where s denotes the entropy density. Now rearranging Eq. (1.7) as $n_\chi = Y_\chi s$ and plugging it in Eq. (1.6) we get,

$$\frac{1}{a^3}\frac{d(Y_\chi s a^3)}{dt} = -\langle\sigma v\rangle[(Y_\chi s)^2 - (Y_\chi^{eq} s)^2], \tag{1.8}$$

where $n_\chi^{eq} = Y_\chi^{eq} s$. It is assumed that for isentropic expansion of the universe, the entropy quantity $S = sa^3$ is conserved [43]. The quantity sa^3 can be taken out of the derivative since it is a constant,

$$\frac{sa^3}{a^3}\frac{dY_\chi}{dt} = -s^2\langle\sigma v\rangle[Y_\chi^2 - (Y_\chi^{eq})^2]. \tag{1.9}$$

(FRW) metric.

[3]This occurs when $\Gamma \sim H$.

Which simplifies to,

$$\frac{dY_\chi}{dt} = -s\langle\sigma v\rangle[Y_\chi^2 - (Y_\chi^{eq})^2]. \tag{1.10}$$

For $T \sim M_\chi$ it is convenient to introduce another quantity given by,

$$x = \frac{M_\chi}{T}. \tag{1.11}$$

To invoke x in Eq. (1.10), we note that

$$\frac{dx}{dt} = \frac{d}{dt}\left(\frac{M_\chi}{T}\right) = -\frac{1}{T}\frac{dT}{dt}\frac{M_\chi}{T} = -\frac{1}{T}\frac{dT}{dt}x. \tag{1.12}$$

But assuming $T \sim a^{-1}$ for the times relevant to the freeze-out, then we get,

$$H = a^{-1}\frac{da}{dt} \sim T\frac{d}{dt}(T^{-1}) = -\frac{1}{T}\frac{dT}{dt}. \tag{1.13}$$

Then we have,

$$\frac{dx}{dt} \simeq Hx. \tag{1.14}$$

The Boltzmann equation in terms of x becomes,

$$\frac{dY_\chi}{dx} = -\frac{s}{Hx}\langle\sigma v\rangle[Y_\chi^2 - (Y_\chi^{eq})^2]. \tag{1.15}$$

But the entropy is given by [43],

$$s = \frac{2\pi^2}{45}g_s T^3, \tag{1.16}$$

where g_s denotes the relativistic effective number of degrees of freedom in entropy. According to [39], we assume a radiation epoch so that $H = H(M_\chi)/x^2$, then Eq. (1.15) becomes the Riccati equation [39, 43, 46],

$$\frac{dY_\chi}{dx} = -\frac{\lambda}{x^2}\langle\sigma v\rangle[Y_\chi^2 - (Y_\chi^{eq})^2], \tag{1.17}$$

where $\lambda = \frac{2\pi^2}{45}g_s\frac{M_\chi^3\langle\sigma v\rangle}{H(M_\chi)}$. The Riccati equation has no closed-form solution, but can be solved in a numerical, or semi-analytical, fashion. The solution to the Riccati equation in the nutshell encapsulate what we discussed before that as long as $\Gamma \gg H$, the Y_χ tracks Y_χ^{eq}, but when $\Gamma \simeq H$ ($x \simeq x_f$), where x_f denotes the freeze-out value of x at the freeze-out temperature T_f, the DM χ particles become so rare that they can no longer maintain thermal equilibrium, subsequently they freeze-out of thermal equilibrium and leave a final relic abundance $Y_\chi^\infty = Y_\chi(x = \infty)$. The Simple analytic approximation to Eq. (1.17) is given by [43],

$$Y_\chi^\infty \simeq \frac{\lambda}{x_f}. \tag{1.18}$$

Expressing the density parameter for DM ($\Omega_\chi = \frac{\rho_{\chi,0}}{\rho_{crit}}$) in terms of Y_χ^∞ gives the DM density in the present day as [39],

$$\Omega_\chi h^2 \sim 0.1 \left(\frac{x_f}{10}\right) \left(\frac{10}{g_s(M_\chi)}\right)^{1/2} \frac{10^{-8}\mathrm{GeV}^{-2}}{\langle\sigma v\rangle}. \tag{1.19}$$

WIMPs with $\langle\sigma v\rangle \sim 10^{-8}$ GeV^{-2} meticulously reproduce the correct DM density, this match is famously known as the "WIMP Miracle"[4].

1.4 Dark Matter Density Distribution

The massive nature of WIMP means that it interacts gravitationally to form a dense DM halo, such that most of the cosmic mass is locked in these halos. In this cold dark matter paradigm, it is assumed that baryonic structure (luminous objects, galaxies, galaxy clusters &, etc) forms in the potential well of the DM halo [47]. In the nutshell, these DM halos are virialized clumps, which resulted from the gravitational clustering around the initial density perturbation within the DM distribution [35, 47]. Properties of these halos play a vital role in the sense that, if the density of WIMPs is augmented, then the probability of the pairs of WIMPs annihilating within that structure is considerably higher than in the smooth medium, since this will be proportional to the square of the density of DM [48]. There exists a multitude of educated guesses to the exact structure of DM density profiles and one of the universal profiles, as suggested by the numerical N-Body simulations, is the Navarro-Frenk-White (NFW) density profile [49, 50],

$$\rho_{NFW}(r) = \frac{\rho_s}{\frac{r}{r_s}\left(1 + \frac{r}{r_s}\right)^2}, \tag{1.20}$$

where ρ_s denotes the characteristic density and r_s denotes the scale radius. It is clear from Eq. (1.20) that when $r \ll r_s$, $\rho(r) \propto r^{-1}$, i.e. a central

[4]The most conventional referenced limit for the thermal relic cross-section as mentioned before is $\langle\sigma v\rangle \simeq 3.0 \times 10^{-26}$ cm^{3}s^{-1}

singularity is present. Another density profile that tends to produce better fits for recent numerical simulation [51, 52] is the Einasto density profile [53],

$$\rho_{Ein}(r) = \rho_s \exp\left\{-\frac{2}{\alpha}\left[\left(\frac{r}{r_s}\right)^{\alpha} - 1\right]\right\}, \tag{1.21}$$

where α denotes the Einasto parameter with 0.17 producing a similar profile to the NFW case for the outer parts of the halo. There exists a possibility of having a smaller α in the modified Einasto profile regime (if the numerical simulations invoke the existence of baryons) [54]. In this dissertation, we will use the contracted Einasto profile where $\alpha = 0.11$. Finally, we have a cored density profile emerging from the observation of rotation curves, called the Burkert profile [55],

$$\rho_{Bur}(r) = \frac{\rho_s}{\left(1 + \frac{r}{r_s}\right)\left(1 + \left[\frac{r}{r_s}\right]^2\right)}. \tag{1.22}$$

Well-measured observations of rotation curves of galaxies suggest that many galaxies seem to have cored density profiles and this is incompatible with cuspy profiles suggested by N-Body numerical simulations [56]. This incompatibility between observations and simulations is known as the "core/cusp problem". This controversy is very evident mainly in dwarf galaxies and low surface brightness galaxies [57].

Cold DM paradigm's N-body numerical simulation suggests that the distribution of DM is not perfectly smooth in the galactic halo due to the presence of substructures (sub-halos) [58, 59]. This is a consequence of hierarchical merging, where smaller halos form first and then merge to form larger structures. But a vast amount of these substructures survive during the hierarchical merging [60]. In essence, sub-halos are denser than the parent galactic halo and this can result in an increase in the number of DM annihilation within the galactic halo. The aforementioned in certain scenarios can easily be taken into account through an effective boost factor that enhances the total DM annihilation rate [61–63].
There exist another two predicaments within the cold DM paradigm concerning the sub-halos. The first issue facing the cold DM paradigm is the missing satellite problem (MSP). In a nutshell, it refers to the overabundance of the N-Body simulation's predicted sub-halos compared to the observation of satellites around the Milky Way. Concisely, simulations suggest that over a thousand sub-halos should, in principle, host dwarf galaxies. But the sensitivity of available surveys only observed ~ 50 dwarf galaxies [64, 65]. A

recent study from [66] elucidate that MSP might be solved if these satellite galaxies that inhabit the Milky Way are characterised by a lower mass of $\sim 10^8 M_\odot$, insinuating they will be inefficient in star-formation due to the effects of reionization and feedback processes. These satellites are not efficient in forming a luminous component, thus making it hard to observe them.
The other predicament worth discussing, which is somewhat related to MSP, is the too-big-to-fail (TBTF) problem, which was initially spotted in the population of satellites that inhabit the Milky Way [67]. If the smallest sub-halos are unable to host the bright Milky Way satellites, it is only natural to assume that more massive/largest sub-halos can. However, simulations predict that the largest Milky Way-like sub-halos are too dense to accommodate the observed kinematics of bright Milky Way satellites [68–70]. TBFT problem is not unique to the Milky Way, it turns out that other galaxies also experience it [71,72]. To date, the TBFT problem is yet to be fully explained, even though several solutions involving the modification of the abundance and internal structure of DM halos due to baryonic processes have attempted to mitigate this problem [73].

1.5 Dark Matter Detection

In order to make sound arguments about proposed solutions to the DM problem mentioned in the previous section 1.2, we would need to be able to detect the DM particles. In this section, we cover three modes of detection: direct detection, collider detection, and indirect detection. Fig. 1.1 gives a schematic representation of all three possible dark matter detection modes.

1.5.1 Direct Detection

This mode of detection was first postulated in the 1980s by the authors of Ref. [75], it involves the possibility of detecting DM particles in a laboratory, this is achieved by identifying nuclear recoils from an elastic scattering between DM particles and a detector's target nucleus. This is shown by the horizontal arrow in Fig. 1.1 and the process is given by the simple equation,

$$\chi + P \rightarrow \chi + P, \tag{1.23}$$

where χ denotes a DM particle and P denotes some standard model particle. Elastic scattering of WIMPs with a mass range $(10-1000)$ GeV are expected to induce nuclear recoils energies within a range of $(1-100)$ keV [76]. This is a low energy interaction and the expected number of events is typically low in such experiments. Hence, a rigorous grasp of variables modulating the

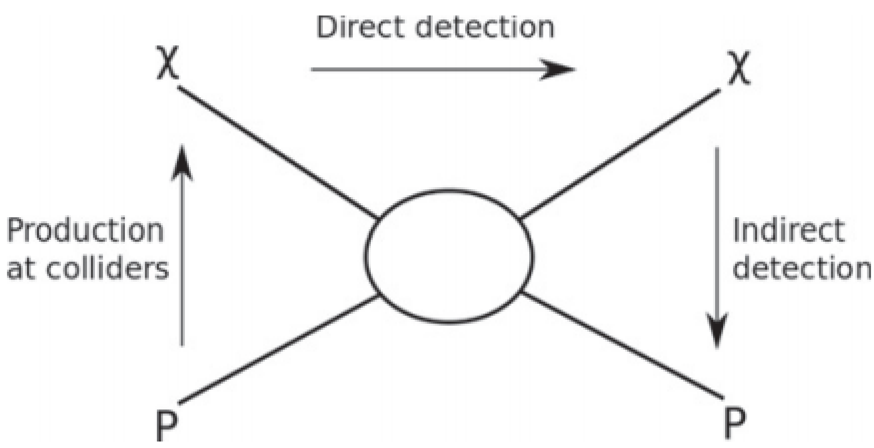

Figure 1.1: Schematic representation of all three possible dark matter detection modes, where χ denotes a DM particle and P denotes some standard model particle. Adapted from [74].

recoils is required and an ultra-sensitive detector characterised by very little background is also needed to detect the events. This is why detectors are normally located deep underground and made of an array of sophisticated cosmic-ray shielding design techniques [77].
The differential recoil spectrum from DM interactions is given by [76],

$$\frac{dR}{dE}(E,t) = \frac{\rho_\chi}{m_\chi m_A}\int v f(\mathbf{v},t)\frac{d\sigma}{dE}(E,v)d^3v, \tag{1.24}$$

where m_χ denotes the DM mass, m_A denotes the mass of the nucleus, ρ_χ denotes the DM local density, $\frac{d\sigma}{dE}(E,v)$ denotes the differential cross-section, v denotes the DM velocity in the detector's rest frame, and finally $f(\mathbf{v},t)$ denotes the DM velocity distribution in the detector reference frame.
In a nutshell, pivotal aspects influencing the experimental sensitivity to DM signal are a combination of energy threshold of the detector, target material, control over the background, and exposure time. For example, through the use of Eq. (1.24), one of the possible DM signatures stems from annual modulations, where the Earth's rotation around the Sun affects the speed of DM particles within the Milky Way halo relative to the Earth. The annual modulations of the DM signal emerge because the Earth's rotation around the Sun in the reference frame of the Milky Way halo is just the superposition of the Earth's rotation around the Sun and the Sun's rotation around the galactic centre of the Milky Way halo. Observations elucidate that the velocity of DM within the Earth's frame is the smallest in Decem-

ber and the largest in June, this further hints that in June that is when a large amount of DM particles induce recoils transcending the detector's energy threshold [78]. Another pivotal factor that can be used to discriminate DM signal over background, is the directional dependence of nuclear recoils. For instance, the Earth's rotation can cause the forward-backward asymmetry of the signal in the preferred recoil direction, hence leading to better discrimination of the DM recoil spectrum over background [79–81]. In the regime of direct detection, the DM-nucleon cross-sections can be divided into spin-independent[5] cross-sections and the spin-dependent[6] cross-sections.

Detectors for direct detection experiments depend on the search for the induction of heat, ionization, and scintillation of light. In heat detectors experiments such as SIMPLE [82], PICASSO [83], COUPP [84] they are characterised by a super-heated instrument occupying a meta-stable state aiming at identifying the DM particle scattering off the target nuclei while depositing some energy, as a consequence phase transition and bubble formation will emerge. Normally, the aforementioned experiments due to their molecular nature they tend to be more sensitive to spin-dependent interactions. For the two-phase (liquid noble gas) detector experiments such as XENON100 (XENON1T) [85, 86], LUX [87], PandaX-II [88] they are characterised by a two-phase time projection chamber that relies on both the mechanisms of scintillation and ionization and typically they are made of a heavy nuclei xenon [7]. The use of xenon makes them more sensitive to spin-independent interactions. We also have cryogenic detector experiments such as EDELWEISS [90], CoGeNT [91], CRESST [92] and others. The first two experiments employ the germanium detector while the latter employs the bolometer/superconducting thermometer detector. The benefit of cryogenic detectors is their ability to permit very low energy thresholds thus allowing the facilitation of better energy resolutions. To date, no experiment is yet to detect any conclusive DM signal but limits have been placed on the DM-nucleon cross-sections as shown in Fig. 1.2. DAMA/LIBRA [93] observed annual modulations of events at 8.9σ significance compatible with the DM interpretation, however, these results are in great contention with other DM experiments [94]. The great confusion in the regime of direct detection further comes from the fact that there exists a mismatch of the DAMA/LIBRA cross-sections and other experiments as shown in Fig. 1.2.

---

[5] Derived from a scalar interaction operator.

[6] Derived from vector/axial-vector interaction operator.

[7] The reasons for using this material stem from the capabilities that offer immense shielding and can also be easily scaled to larger masses [89].

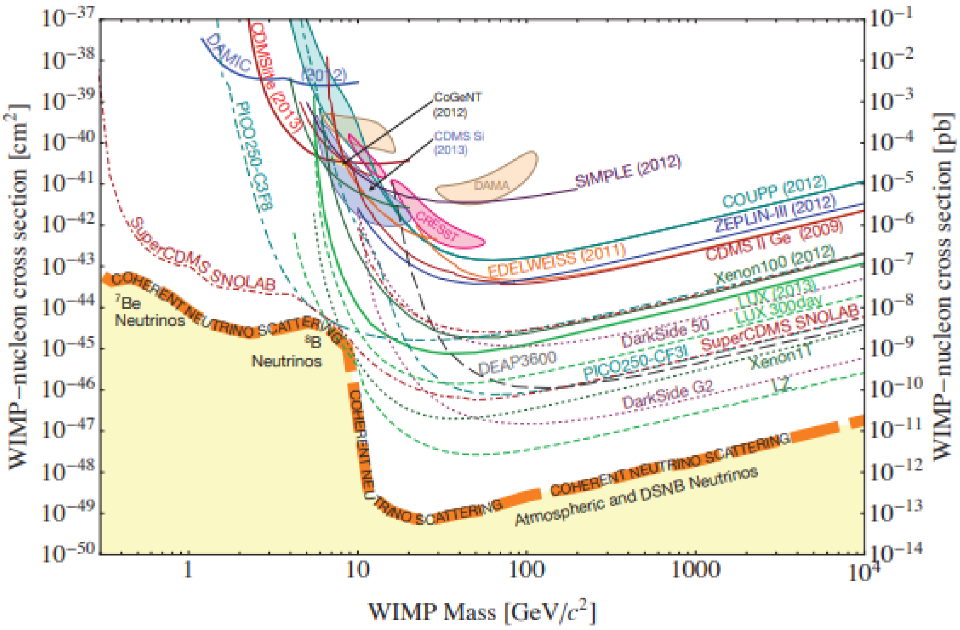

Figure 1.2: A compilation of current limits (solid lines) on the DM-nucleon spin-independent cross-sections and hints of DM signals (closed contours) from various experiments and the projection (dashed) for the next generation of direct dark matter experiments. The orange dashed line shows the neutrino floor. Adapted from [94].

1.5.2 Collider Detection

This mode of detection involves the possibility of producing DM particles in accelerators by colliding particles at higher speeds. The process is denoted by the arrow pointing upwards in Fig. 1.1 and is given by the equation,

$$P + P \rightarrow \chi + \chi. \tag{1.25}$$

We assume that there exists coupling between P and χ. Such events are undetectable since DM particles (e.g WIMPs) interact weakly with baryonic matter. However, they can be traced/reconstructed from the products of the collision (photons, jets, heavy boson) and an imbalance of various quantities in the transverse plane, such as the missing transverse energy and momentum. A sensible approach is to choose events with large missing energy such as the standard model background is reduced and the DM signal can be disentangled. One thing that distinguishes this mode of detection from the rest is the lack of astronomical uncertainties. One experiment at the forefront of collider search for DM is the LHC. The LHC can probe the important ranges of parameter space of DM at the GeV-TeV scale [95]. To date, there exists no direct evidence of DM, but there exist increasingly stringent limits (placed by the LHC) on the properties of DM [96]. In near future, the LHC may be able to shed some light on the nature of DM, and also in a near future, an experiment called International Linear Collider (ILC) is expected to place more stringent limits on the DM mass and relic density plane [97]. For now at the LHC, two experiments ATLAS [98] and CMS [99] investigate the high energetic proton-proton collisions. However, the production of DM particles is expected to be rare in collisions. To circumvent this impediment, larger luminosity [8] is required, luckily this is one of the strongest traits of the LHC. Depending on the choice of the particle physics model, various techniques can be employed to constrain the parameter space of the model. Assuming crossing symmetry, limits emerging from DM particle (e.g. WIMPs) production cross-section can be translated into limits on nucleon-WIMP scattering cross-section, this allows the comparison to the limits from direct DM detection. Fig. 1.3 elucidate constraints on the nucleon-WIMP cross-section from the CMS [100] and ATLAS [101], these are compared to the direct detection experiment constraints. Firstly, in Fig. 1.3 the best CMS limits are apparent for DM mass below 3.5 GeV/c^2, a region that is yet to be explored by direct detection experiments. Secondly, small WIMP masses below 10 GeV produce ATLAS limits that are highly competitive or substantially better compared to those set by direct DM detection limits.

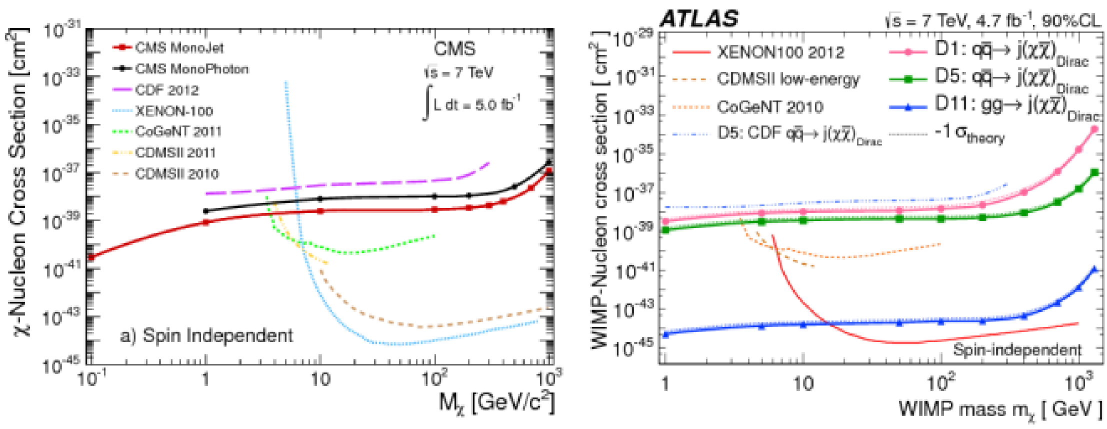

Figure 1.3: Derived limits for spin-independent nucleon-WIMP cross-section from collider data. Left: Denote limits from CMS experiment [100]. Right: Denote limits from ATLAS experiment [101].

[8] This is a quantity that quantifies the number of collisions per unit time

1.5.3 Indirect Detection

This mode of detection is executed by seeking SM products induced from DM annihilations or decays within DM-rich environments. Optimal targets are locations with high DM density, and this includes the Milky Way's galactic centre/halo, close-by galaxy clusters, and spheroidal dwarf galaxies[9]. This mode of detection is depicted by the vertical arrow pointing downwards in Fig. 1.1 and the process is given by the simple equation,

$$\chi + \chi \rightarrow P + P. \tag{1.26}$$

Concisely, what transpires is that DM particles annihilate into various SM channels. Subsequently, after annihilations, these products decay, hadronise or go through the process of showering to produce stable particles such as positrons, electrons, antiprotons and gamma rays. Because of the propagation of the stable particles some signals may be detected at the location of the Earth in a form of annihilation products or secondary emissions. The secondary emission can be in terms of radio, gamma-ray, or X-ray emission depending on the mechanism of interest, in our case this is radio emission. The injection of stable particles i into DM halo environments is described by the source function Q, which is characterised by the dependence of the position within the DM halo r and the energy E of the stable particles i. For annihilation, it is given by,

$$Q_{i,A}(E,r) = \frac{1}{2}\langle\sigma V\rangle \sum_f \frac{dN_i^f}{dE} B_f \mathcal{N}_\chi(r), \tag{1.27}$$

where $\langle\sigma V\rangle$ denotes the thermally velocity-averaged DM annihilation cross section at $0K$,f denotes the kinematically allowed annihilation states with the branching ratio B_f, $\frac{dN_i^f}{dE}$ denotes the production spectra for the stable particle i, and the $\mathcal{N}_\chi(r) = \frac{\rho_\chi^2}{M_\chi^2}$ (where M_χ, ρ_χ denote the DM mass and density respectively) yields the DM pair density at the given radius r within the DM halo.
For decay it is given by,

$$Q_{i,D}(E,r) = \Gamma \sum_f \frac{dN_i^f}{dE} B_f n_\chi(r), \tag{1.28}$$

where Γ denotes the decay rate for DM, f in this case denotes the allowed decay states with the branching ratio B_f, $\frac{dN_i^f}{dE}$ denotes the production spectra

[9]This is mainly preferred due to the large measured mass to light ratio and the small background detected.

for the stable particle i, and finally $n_\chi(r) = \frac{\rho_\chi}{M_\chi}$ yields the number density of DM at a certain radius r within the DM halo. Q in both Eq. (1.27) and (1.28) has the dimensions of number of particles i induced per unit volume per unit energy, per unit time.

The best-injected DM annihilation products to hunt or probe are gamma rays and this is solely because of their propagation nature. In essence, gamma rays are characterised by a null charge. Hence, they propagate freely without being perturbed thus making it a simple duty to disentangle and trace their origin. However, gamma rays can be affected by absorption in the interstellar medium. The generation of electron-positron pairs in photon-photon interactions ($\gamma\gamma \rightarrow e^+e^-$) is the physical mechanism generating absorption of gamma-rays in the interstellar medium. Detectors such as the Fermi-LAT [102] along with a multitude of ground-based imaging Cherenkov telescopes (IACTs)[10] have attempted to observe the DM annihilation or decay products. To date, HESS [103], VERITAS [104] and MAGIC [105] have placed stronger bounds on the self-annihilation cross-section of DM. Though the planned CTA [106] for the next generation of instruments will possess a depth able to probe the underlying parameter spaces for particle physics models, this will be executed in such a way complementary to both the direct and collider DM search [107].

Another possibility of indirect DM detection is through the probing of cosmic ray propagation, especially anti-particles since only a few processes are responsible for their production. The cosmic rays are immersed in a turbulent galactic magnetic field, hence unlike gamma rays their propagation is perturbed, i.e. they take random walks. Due to the random walks, the propagation of the cosmic rays, in a nutshell, is described as a diffusion process from an extended source (the DM halo) to some final destination (in our case is the Earth's location) [108]. During the journey of the diffusion process, the cosmic rays experience several other processes, and in particular the energy loss process due to nuclear spallation, Coulomb scattering, synchrotron radiation, inverse Compton scattering, and bremsstrahlung. The putative approach for solving the transport equation for cosmic rays is through numerical and semi-analytical solution codes (GALPROP [109] and DRAGON [110]), because these codes have successfully reproduced the cosmic ray abundance under the assumptions from Fermi acceleration theory. HEAT [111], MASS [112], PAMELA [113], AMS-02 [23], and DAMPE [114] have reported excesses in the cosmic rays, and several explanations account for these excesses using DM models. Although other explanations use astrophysical sources such as

[10] These search for Cherenkov light induced by gamma rays whenever they interact with the Earth's atmosphere.

a pulsar [115, 116], to explain the excesses.

1.5.4 The MeerKAT Telescope

Detectors used for indirect detection traditionally include the gamma-ray experiment, Fermi-LAT [102] because this mode of detection is characterised by low attenuation in the interstellar medium and it has high detection efficiency [117]. Recently indirect hunt for DM annihilation induced particles in radio-band has been prominent, this emerges from the fact that radio interferometers have an angular resolution transcending that of gamma-ray experiments. The regime of hunting DM in the radio-band was advocated by Ref. [118] for Draco dwarf galaxy and ever since the field has been active in constraining DM models. Furthermore, there has been also some previous suggestion of searching DM-induced radio signals in galaxy clusters like Coma (See Ref. [119]). Initial studies of indirect radio-band search for DM were conducted using the Australia Telescope Compact Array (ATCA), to probe the DM-related diffuse radio emission from dwarf galaxies [120]. The shortcoming that such experiments face is unknown magnetic field environments. Since ATCA was inadequately sensitive to perform μG rotation measure probes, the produced limits suggested that a far more sensitive instrument like MeerKAT might prove to be more useful in probing far fainter flux levels, to improve the limits for DM particle properties. Indeed, MeerKAT sensitivity is around a factor of 2 better than ATCA. The sensitivity of MeerKAT makes it undoubtedly one of the leading tools in the hunt of DM, since it will allow the probing of far fainter DM halo targets. MeerKAT is currently operated by the South African Radio Astronomy Observatory (SARAO) and it is the precursor of the Square Kilometre Array (SKA) mid-frequency band. SKA is a long-term international radio telescope project being built in both Australia and South Africa. The goal of the project is to develop the largest radio telescope with a collecting area of about a square of a kilometer. Furthermore, SKA offers 50 times more sensitivity and 10, 000 times survey speed of the best current radio instruments. Presently, MeerKAT is constituted by 64 antennas, where each antenna is characterised by a 13.5 m diameter dish and equipped with L-band cryogenic receivers. Additionally, the antennas are configured in such a way that provides high sensitivity, superior radio frequency interference rejection as well as a wide imaging coverage range of the sky. MeerKAT is expected to get an upgrade of 20 more dishes, taking it to 84, and this is expected to be achieved by 2023 [11]. Point source sensitivity of 2.45 μJy beam^{-1} at robust weighting 0 is possible with just 20

[11] https://www.mpg.de/15382572/top-radio-telescope-in-south-africa

hours MeerKAT observation time[12]. Taking into consideration the synthesized beam size of ≈ 11 arcseconds and assuming arcmin scale emission, the rms sensitivity is given by,

$$\text{rms sensitivity} = 2.45\ \mu Jy\ \text{beam}^{-1} \times \left(\frac{1\ \text{arcminute}}{11\ \text{arcseconds beam}^{-1}}\right)^2 \approx 73\ \mu Jy. \tag{1.29}$$

However, we do note that 73 μJy is a more conservative estimate since tapering is elided in this work. Tapering on the arcminute scale can potentially improve the MeerKAT sensitivity since the DM diffuse emission will be found on the arcminute scale [121] while visibility taper down-weights contributions from long array baselines [122], naturally, this occurs at smaller angular scale and this is where point sources dominate the signal.
To get the conservative SKA sensitivities, we employ values from Tables 6 and 7 from Ref. [123] and an analogous scaling to get arcmin^{-2} similar to MeerKAT, however, we make use of the geometric mean quoted minimum and maximum beam sizes.

[12]We refer the reader to https://archive-gw-1.kat.ac.za/public/tools/continuum_sensitivity_calculator.html for the visualization of the sensitivity.

Chapter 2

Madala Hypothesis

In the previous chapter, we described DM scientific case in a model-independent way but since we are working in a model-dependent way, we introduce our particle model (Madala hypothesis). The motivation for extension of the standard model and the establishment of the Madala hypothesis are discussed along with the current limits placed by the LHC data. Finally, we introduce the DM annihilation channels offered by our model.

2.1 Standard Model

Standard Model (SM) is a successful quantum field theory incorporating known elementary particles and their associated interactions. The model is built from observations that essentially correlate and predict data [124]. It describes three fundamental forces: the strong, weak, and electromagnetic force, but does not include the gravitational force. All elementary particles in the universe can be subdivided into two groups: fermions and bosons. Fermions are characterized by half-integer spin, and bosons are characterized by an integer spin. In total, there are 12 spin $\frac{1}{2}$ fermions along with their anti-particles classified according to how they interact in the SM. There are also spin 1 gauge bosons which serve as mediators for strong, weak, and electromagnetic interactions. Each fundamental force is characterised by a unique gauge boson, for electromagnetism we have a "photon", for the strong force we have "gluons" and finally for the weak force we have "vector bosons ($W^{\pm}$ and Z)". It is worth noting even for gravity there is postulated boson called graviton. Fig. 2.1 summarises the SM model along with its particles.

Fermions constitute two groups (quarks and leptons). In total, there are six quarks (up, down, charm, strange, bottom, top) and six leptons (electron, muon, tau, electron neutrino, muon neutrino, tau neutrino). Quarks

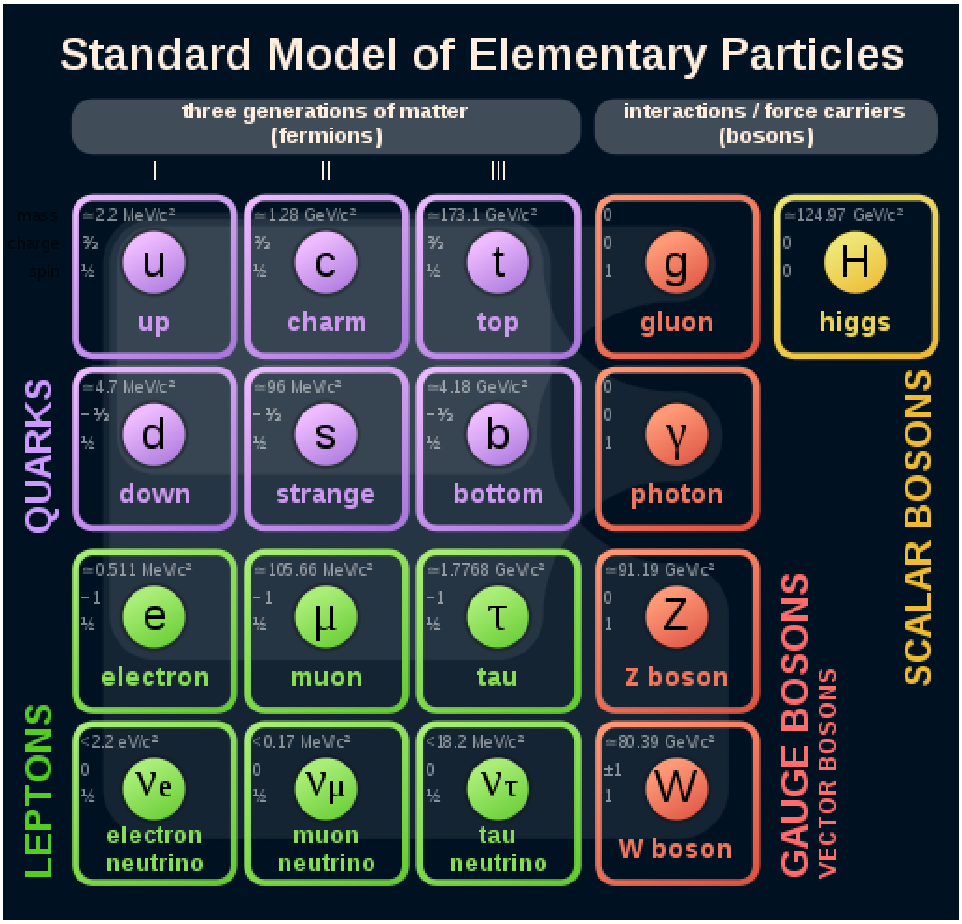

Figure 2.1: Schematic diagram of the Standard Model particles [125].

carry both electric and colour charge and are rarely free, that is they always occupy a bound state at low energies, this phenomenon is known as confinement. On the other hand, electron, muon and tau carry an electric charge while the neutrinos have a null charge. Furthermore, neutrinos can have a smaller mass due to a consequence of the phenomenon of neutrino oscillations and they materialize as missing energy in colliders since they only interact weakly. The vector bosons ($W^{\pm}$ and Z) are massive and collectively with photons at electroweak scale at $\mathcal{O}(100\text{ GeV})$ can mediate electroweak interactions (the unification of the electromagnetism and weak force). Naturally, the aforementioned regime of low energy is where SM operates and exhibits more success. Finally, in SM we have a spin 0 boson called the Higgs boson h. h explains how elementary particles acquire their mass through a process called the Higgs mechanism. This boson was only discovered recently in 2012 by CMS and ATLAS experiment at the LHC through Run-1 data [126, 127]. The discovery laid a foundation for the understanding of notions such as electroweak symmetry breaking (EWSB). Global fits to the data suggest properties that are consistent with the expectations from the SM. The discovery of the Higgs boson means the particle spectrum of the SM is complete. As much as SM to date is regarded as one of the successful theoretical frameworks it, unfortunately, faces some shortcomings. SM cannot cater for gravity, oscillation of neutrinos [128], baryonic asymmetry [129] and the dark sector of the universe. As a consequence, in the particle physics community the SM is considered as a low energy limit for a more sophisticated and fundamental theory. To date, there exists a multitude of beyond standard model (BSM) theories, and in this work, we will discuss such a type of theory called the Madala hypothesis.

2.2 Why Do We Need the Madala Hypothesis?

The madala hypothesis extends the Higgs-sector of the SM by introducing bosons heavier than SM h. The bosons introduced are the Madala boson[1] H and scalar mediator S. H is characterised by a mass range of $2m_h < m_H < 2m_t$, where m_h, m_H, m_t are the SM Higgs boson mass, Madala boson mass, top quark mass respectively [18, 130]. Meanwhile S serves as portal between SM particles and the dark sector (or DM candidate), it has mass within a range $m_h < m_S < m_H - m_h$ [131]. In essence the model was postulated to explain the anomalous features seen in Run-1 [16,131] and Run-2 data [17] at the LHC. The particular anomalies include the Higgs boson's transverse momentum p_T and the event excesses in the multi-leptons final states [16, 18, 130–132]. According to Ref. [133] 8.04σ combined significance for the multi-lepton excesses can be reached. Recently, the significance is augmented past 10σ [134, 135].

One of the remarkable predictions made by the Madala hypothesis is that through a decay mode of H where at least one h is produced, i.e. $H \to hh, h\,\chi\chi$, the apparent distortion of h's transverse momentum spectrum from differential distribution of ATLAS Run-1 data [136, 137] can be explained. Interestingly, the Madala hypothesis also provides a DM candidate χ which would manifest as a consequence of the decay mode of H which is seen as a production of the Higgs boson associated with missing energy. Simply

[1] "Madala" is a zulu word used to refer to an old person, hence the connotation suggests that Madala boson is old and heavier than the SM Higgs boson.

introducing H can account for excesses in the production of h in association with top quarks, observed by both ATLAS and CMS [131]. S was introduced to explain the effective decay vertex, and the preferential decay mode of H is given by $H \to SS, Sh, hh$. In a nutshell, S is kinematically accessible through the aforementioned decay modes of H. Furthermore, S is assumed to have SM Higgs-like couplings [16, 131]. Fig. 2.2 summarises the effective vertex along with the cascading decay process for the production of the Higgs boson.

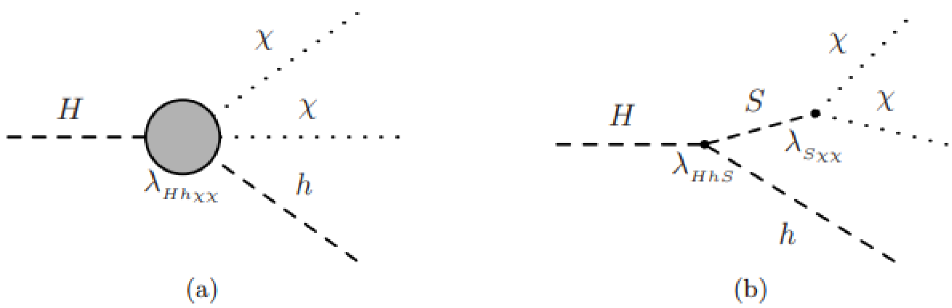

Figure 2.2: Decay mode of H as Feynman diagrams, where (a) depicts the effective vertex and (b) depicts the decay of S [131].

The mass of the Madala boson was constrained through the computation of the minimized χ^2 for the anomalous features in the Run-1 LHC data against the χ^2 of the Madala hypothesis, as seen in Fig. 2.3. The 3σ best fit requires that $m_H \approx 270$ GeV. The parameters of the Madala hypothesis are fixed such that $m_S = 150$ GeV and assuming the dominance of the decay mode $H \to Sh, SS$ [17].

2.3 Madala Hypothesis as a Two-Higgs-Doublet Plus Scalar Singlet Model

The Madala hypothesis is considered as a two-Higgs-doublet model (2HDM) since it introduces additional bosons. However, the 2HDM model alone is not adequate to accommodate features seen in the LHC data. This advocates the extension of 2HDM model by introducing a real singlet scalar S [2]. Thus, the

[2] The real singlet scalar is neutral under the standard model gauge group.

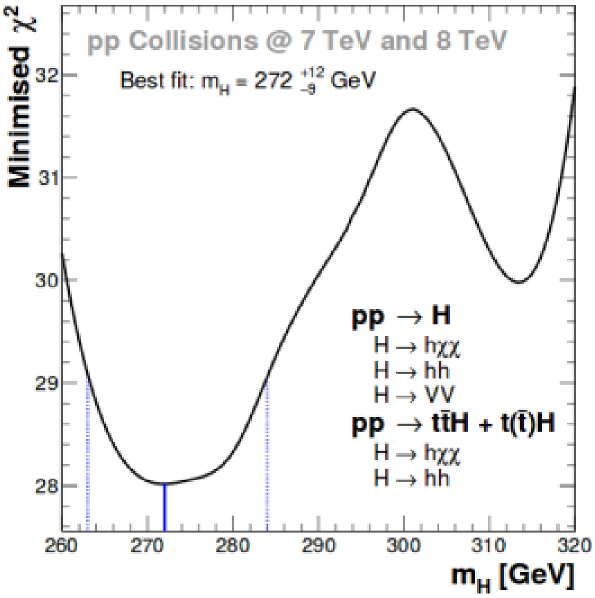

Figure 2.3: The minimised χ^2 as a function of the mass of Madala boson m_H [16].

Madala hypothesis is considered as a 2HDM+S model instead. The beauty of the 2DHM+S model is that it can be explored with DM scenarios and can produce the anomalous multi-leptons seen at the LHC [131]. When the Madala hypothesis is compared to data [17], the revelation is that there exists large discrepancies between the SM Monte-Carlo and data. Unfortunately, such discrepancies transcend the current understanding of the theoretical systematics. The embedding of the Madala hypothesis into a 2HDM+S model is perpetually improving and tested by experiments, with further analysis this can potentially improve our understanding of the discrepancies in the multi-lepton final states. Recently, the Madala hypothesis is tested using the $\gamma\gamma$ and $Z\gamma$ data, furthermore, this type of approach provides 5σ evidence for the existence of the real scalar singlet S [135]. Following Ref. [138], the CP-conserving potential of the two Higgs-doublet model with an additional real singlet scalar field Φ_S is given by,

$$
\begin{aligned}
&V(\Phi_1, \Phi_2, \Phi_S) \\
&= m_{11}^2 \left|\Phi_1\right|^2 + m_{22}^2 \left|\Phi_2\right|^2 - m_{12}^2 \left(\Phi_1^\dagger \Phi_2 + \text{h.c.}\right) \\
&+ \frac{\lambda_1}{2} \left(\Phi_1^\dagger \Phi_1\right)^2 + \frac{\lambda_2}{2} \left(\Phi_2^\dagger \Phi_2\right)^2 + \lambda_3 \left(\Phi_1^\dagger \Phi_1\right) \left(\Phi_2^\dagger \Phi_2\right) \\
&+ \lambda_4 \left(\Phi_1^\dagger \Phi_2\right) \left(\Phi_2^\dagger \Phi_1\right) + \frac{\lambda_5}{2} \left[\left(\Phi_1^\dagger \Phi_2\right)^2 + \text{h.c.}\right] \\
&+ \frac{1}{2} m_S^2 \Phi_S^2 + \frac{\lambda_6}{8} \Phi_S^4 + \frac{\lambda_7}{2} \left(\Phi_1^\dagger \Phi_1\right) \Phi_S^2 + \frac{\lambda_8}{2} \left(\Phi_2^\dagger \Phi_2\right) \Phi_S^2. \qquad (2.1)
\end{aligned}
$$

Both fields Φ_1 and Φ_2 denote $\mathrm{SU(2)_L}$ Higgs doublets. Φ_S is characterised by a real non-zero vacuum expectation value to allow mixing across all the CP-even neutral states. λ_S is the singlet quartic couplings. λ_i is considered to be real and this amounts to a model which has no explicit CP-violation. The first two lines terms of Eq. (2.1) emerge from the real 2HDM potential, while the last line terms are a consequence of the introduction of the singlet field Φ_S. To mitigate the tree-level flavour changing neutral current (FCNC), all quarks with a given charge must couple to a single Higgs doublet. This is executed by imposing $\mathbb{Z}_2$ symmetry which can be softly broken by $m_{12} \neq 0$. Also, through the extension $\mathbb{Z}_2$ symmetry to Yukawa sector guarantees the absence of FCNC at tree-level [138]. After minimization of the potential and spontaneous EWSB, 2HDM+S Higgs sector constitutes of six Higgs particles: three CP-even scalars h, H and S, one charged Higgs pair $H^{\pm}$, one CP-odd scalar A. We refer the reader to Ref. [131,138] for a more detailed approach of the model along with associated Lagrangians of the interactions as well as the parameter space.
In this work we consider the interaction of S with three DM candidates χ_r, χ_d and χ_v characterised by spin 0, 1/2 and 1, respectively. The interactions is given by,

$$
\begin{aligned}
\mathcal{L}_{int} = &\frac{1}{2} M_{\chi_r} g_{\chi_r}^S \chi_r \chi_r S + \bar{\chi_d}(g_{\chi_d}^S + i g_{\chi_d}^P \gamma_5) \chi_d S \\
&+ g_{\chi_v}^S \chi_v^\mu \chi_{v\mu} S, \qquad (2.2)
\end{aligned}
$$

where g_{χ_i} gives the coupling strength between the DM candidates and the real scalar S. M_{χ_i} denotes the masses of DM candidates. One of the aim of this work is to employ the Madala hypothesis to interpret the astrophysics excesses (AMS-02 and Fermi-LAT), so we focus on the DM annihilation channel through S following $2 \to 2$ and $2 \to 3$ scattering. The $2 \to 2$

corresponds to the scattering process $\chi\bar{\chi} \to S \to X$ while $2 \to 3$ corresponds to $\chi\bar{\chi} \to S \to HS/h \to X$ (where X corresponds to SM products such as positrons, anti-protons and photons). The non-DM parameters are fixed according to Ref. [17,131]. To limit the minimum DM mass considered, we only focus on interactions whereby 2HDM+S virtual particles are not produced. It is worth noting that in this work, we have not considered the thermodynamics of the Madala hypothesis, hence, we assume that in principle the creation of TeV chi particles would take place when the early universe was sufficiently hot for H to decay into χ's.

2.4 Annihilation Yield Functions Generated Via the Madala Hypothesis

In this section we discuss the per-annihilation yield functions $\frac{dN_i}{dE}$ of positrons, anti-protons and photons generated via Monte Carlo (MC) event generators. Employing the Madala hypothesis, the production of particles as a result of DM annihilation through the scalar mediator S are simulated via MC generators. The primary tool used to generate $2 \to 2$ and $2 \to 3$ scattering processes is **MG5_@MC** [139]. In order to hadronize the intermediate partons, the MC generator was interfaced with **Pythia 8** [140]. In this work, the DM mass range varied between 75 to 1000 GeV for the $2 \to 2$ scattering and 200 to 1000 GeV for the $2 \to 3$ scattering with 100 GeV spacing.

Fig. 2.4 displays a complete set of yield spectra for positrons, anti-protons and photons for the $2 \to 2$ and $2 \to 3$ scattering. In the nutshell, these graphs exhibit the number of particles per annihilation per unit energy, $\frac{dN_i}{dE}$, along with the yield functions binned in energy intervals of 0.5 GeV. We only demonstrate spin-0 DM results since there is no significant difference in the yield functions per annihilations for other spin choices. However, we observe that the cross section for the $2 \to 3$ process is a several orders of magnitude smaller than that of $2 \to 2$ case.

2.4.1 Comparison to Other Annihilation Channels

In this section, we discuss the comparison of the Madala hypothesis induced differential yield functions to other commonly used annihilation channels, this includes the μ lepton, τ lepton, b-quark, and Higgs channels from Ref. [141]. In general, these annihilations take the form described by Eq. (1.26). It is worth highlighting that for each scattering only the minimum and maximum

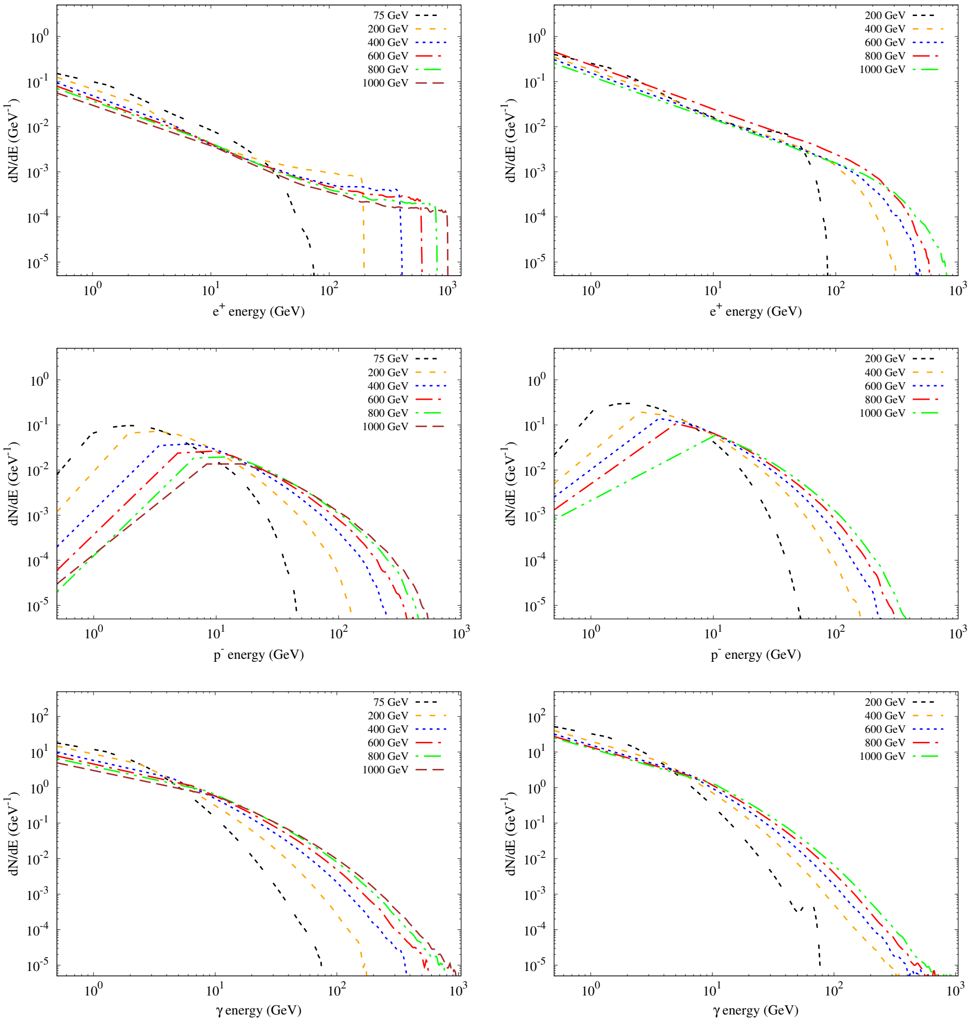

Figure 2.4: Differential yields of positrons, anti-protons and photons for the 2→2 (Left graphs) and 2→3 (Right graphs) annihilation scattering of Spin-0 DM masses [1]. Model parameters are fixed according to Refs. [17, 131], based on LHC data.

masses are shown, i.e. for $2 \to 2$ we have 75 and 1000 GeV while for $2 \to 3$ we have 200 and 1000 GeV. In Fig. 2.5, the photon spectral comparison is shown. For $2 \to 2$, we observe that for 75 GeV, the photon yields produced exceeds all the other channels at lower energies. However, as the energy is augmented the photon yields decline until a spectral cut-off. For 1000 GeV, the $2 \to 2$ photons induced per annihilation behaves similarly to the Higgs channel. Similarly, for $2 \to 3$ induced photon yields exceeds all other channels at lower energies, and at higher energies the photon yield drops substantially below all other channels for 200 GeV. Interestingly, for 1000 GeV, we see weaker photon yields being produced for low energies. In Fig. 2.6, the anti-proton spectral comparison is displayed. The $2 \to 2$ anti-protons yields produced for 75 GeV centre together with the b-quarks and Higgs channel at lower energies and continues to transcend all other channels at higher energies just before a cut-off. In contrast, for 1000 GeV, the anti-proton yields produced transcend all other channels at higher energies. The $2 \to 3$ anti-proton yields induced for 200 GeV only exceed the τ and μ leptons channels just before a cut-off. Even for 1000 GeV, the anti-protons yields exceed the τ and μ leptons by at least an order of magnitude, and it is superior to all other channels at high energies.

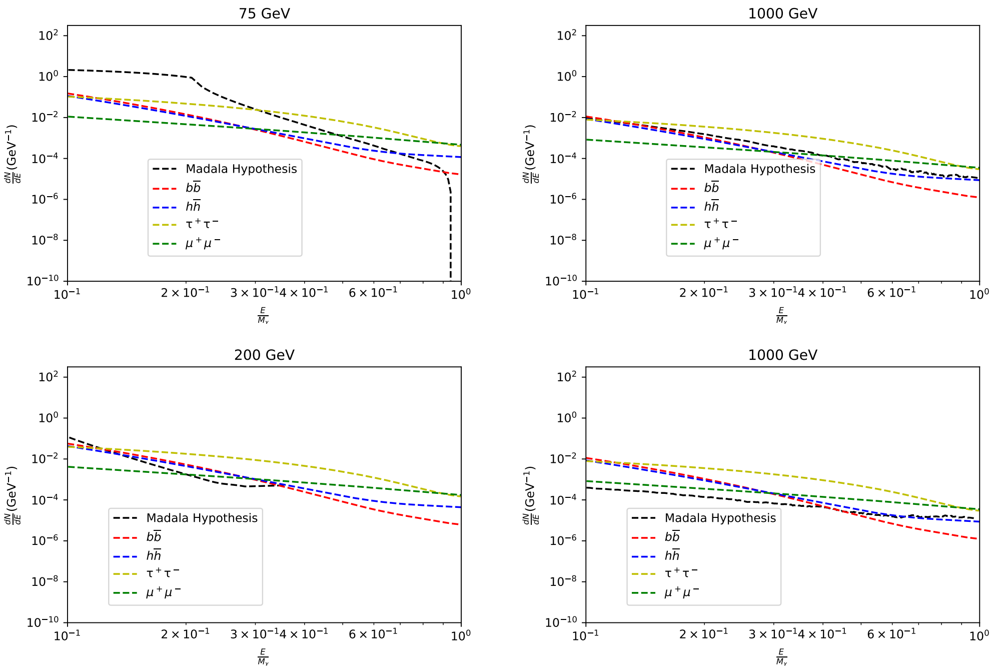

Figure 2.5: Madala hypothesis photon spectral comparison with μ leptons, τ leptons, b-quarks and Higgs channels. Top: $2 \to 2$ scattering. Bottom: $2 \to 3$ scattering.

In Fig. 2.7, the positron spectral comparison is shown. For $2 \to 2$ the 75 GeV positron yield behaves like the Higgs channel just before a cut-off at high energies. Meanwhile, for 1000 GeV we have a harder spectrum that is weaker at low energies but stronger at higher energies compared to other channels. However, for $2 \to 3$ the 200 GeV is comparable to the leptonic channels before a cut-off. In the 1000 GeV case there is only a similarity to τ leptons at lower energies. The apparent difference between the three cases (photons, anti-proton, and positrons) of the comparison, is that the spectral cut-off for lower masses (75 and 200 GeV) is much harsher for the anti-protons yield spectra. Furthermore, for lower masses, the yields of all channels tend to centre together at lower energies.

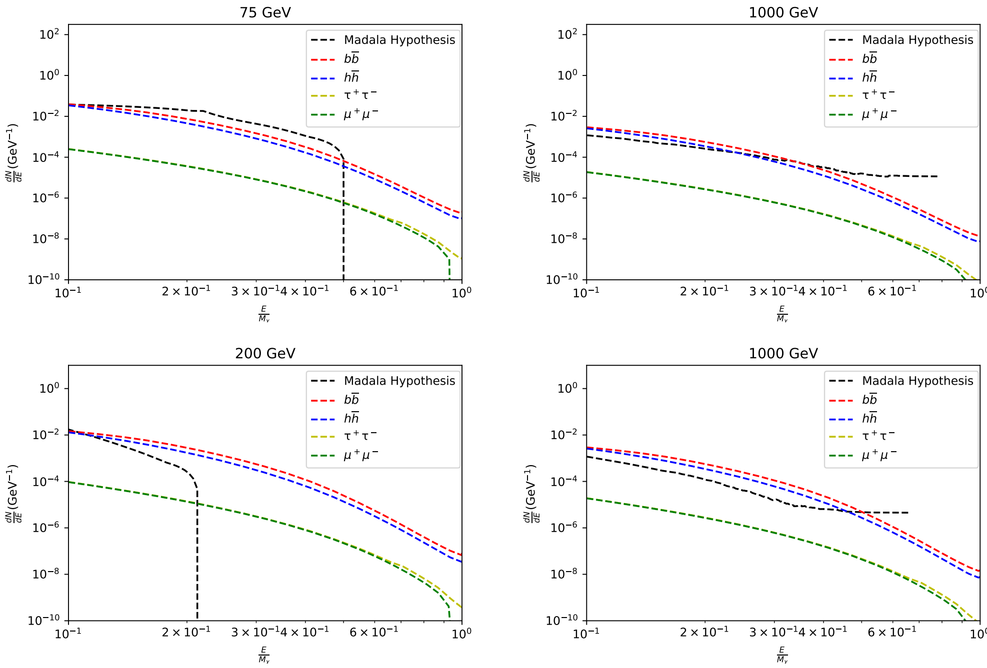

Figure 2.6: Madala hypothesis anti-proton spectral comparison with μ leptons, τ leptons, b-quarks and Higgs channels. Top: $2 \rightarrow 2$ scattering. Bottom: $2 \rightarrow 3$ scattering.

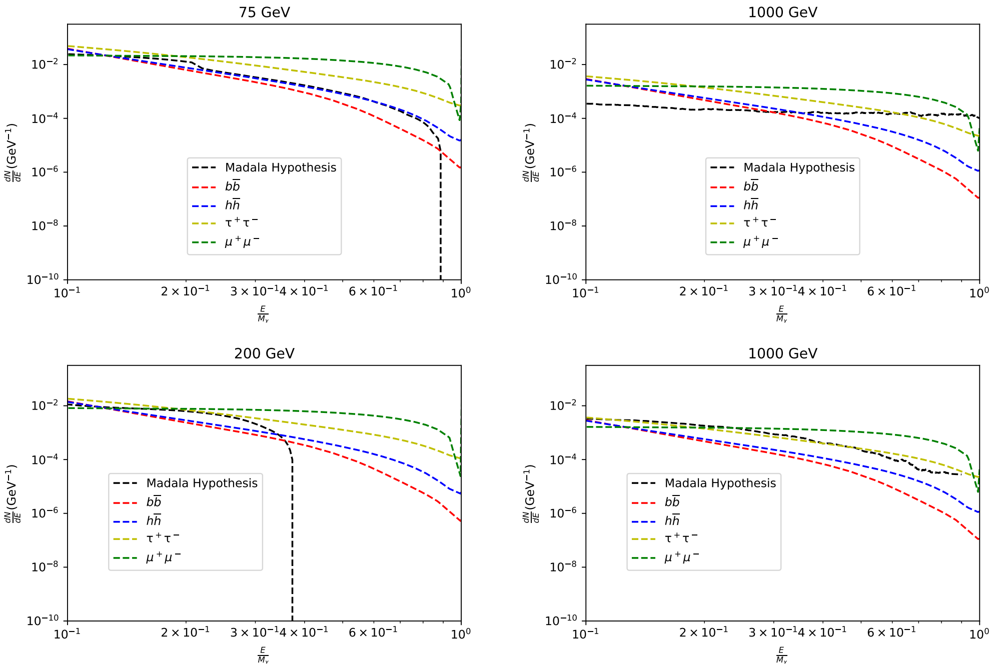

Figure 2.7: Madala hypothesis positron spectral comparison with μ leptons, τ leptons, b-quarks and Higgs channels. Top: $2 \rightarrow 2$ scattering. Bottom: $2 \rightarrow 3$ scattering.

Chapter 3

Cosmic Rays and Gamma Rays Propagation

In this chapter, we will discuss how cosmic rays and gamma rays propagate from the galactic centre to the Earth. We consider the DM annihilation through S according to $2 \to 2$ and $2 \to 3$ scattering as discussed in Chapter 2.

3.1 Positrons Propagation

We are interested in how the positrons produced by the DM annihilation propagate from the Galactic Centre (GC) to Earth. In general, charged cosmic rays propagate through the galactic magnetic field and are scattered by its irregularities. The aforementioned results in the diffusion of charged cosmic rays. Our galaxy is characterised by the presence of a turbulent and tangled magnetic field, as a consequence the produced positrons will follow random walks within the galactic halo, i.e. not all the positrons reach us on Earth. The random walk propagation of positrons can be modelled using the standard diffusion-loss equation,

$$\frac{\partial}{\partial t} f(E,\vec{x}) = \nabla(\mathcal{K}(E,\vec{x})\nabla f(E,\vec{x})) + \frac{\partial}{\partial E}[b(E,\vec{x})f(E,\vec{x})] + Q_{e^+}(E,\vec{x}), \quad (3.1)$$

where $f(E,\vec{x}) = \frac{dN_{e+}}{dE}$ is the number density per unit energy for positrons, $\mathcal{K}(E,\vec{x})$ is the diffusion coefficient due to the turbulent magnetic field, $b(E,\vec{x})$ is the energy-loss factor due to several processes such as synchrotron emission and inverse Compton scattering with the Cosmic Microwave Background (and optical or infrared photons from the galactic stars), finally $Q_{e^+}(E,\vec{x})$ is the source term that injects the positrons into the galactic halo. For annihilations, the source term is given by [142],

$$Q = \frac{1}{2}\left(\frac{\rho_\chi(\vec{x})}{M_\chi}\right)^2 \langle\sigma V\rangle_f \sum_f \frac{dN^f_{e^+}}{dE}, \quad (3.2)$$

where the factor $\frac{1}{2}$ eventuates from the pair annihilations of the identical particles, $\langle\sigma V\rangle$ denotes the thermally velocity-averaged annihilation cross-section for DM particles, $\frac{dN^f_{e^+}}{dE}$ denotes the production spectra for the positrons, the factor $(\frac{\rho_\chi}{M_\chi})^2$ (Where M_χ, ρ_χ denote the dark matter mass and density respectively) yields the dark matter pair density at the given position $\vec{x}$ within the galactic halo. For a given annihilation channel, f runs over all the channels in the final states. It is worth noting that $\mathcal{K}(E,\vec{x})$ depends on assumptions about the Milky-Way diffusion environments [141]. According to Ref. [141] in principle $\mathcal{K}$ has a spatial dependence since there are changes throughout the galactic halo for the distribution of the diffusive inhomogeneities of the magnetic field. However, the construction of a detailed map of such variations is prohibitive since it largely depends on poorly known local galactic geography. Since we adopt the formalism from Ref. [141], we take the parameterization of the diffusion coefficient as $\mathcal{K}(E,\vec{x}) = \mathcal{K}_0(\frac{E}{\text{GeV}})^\delta$, where $\mathcal{K}_0$ and δ denotes the propagation parameters.
We are interested in the positron's equilibrium density to represent the result of DM annihilations occurring over a long period of time, hence the Eq. (1.1) can be easily solved for a steady state condition $\frac{\partial f}{\partial t} = 0$. Then Eq. (1.1) becomes,

$$\mathcal{K}(E,\vec{x})\nabla^2 f(E,\vec{x}) + \frac{\partial}{\partial E}[b(E,\vec{x})f(E,\vec{x})] + Q_{e^+}(E,\vec{x}) = 0. \quad (3.3)$$

The trick is to solve the equation in a diffusion zone with a shape of a solid flat cylinder that engulfs the galactic plane, with height $2L$ in the z-direction and radius $R = 20$ kpc in the radial direction [143, 144]. Imposing the free escape boundary condition implies that the positron density f drops to zero on the surface of the cylinder [145,146]. There exist three sets of models that are widely used in literature to infer the propagation parameters $\mathcal{K}$, δ and L. The models yield a best-fit to the Cosmic rays boron to carbon (B/C) ratio data [147], the values are summarized in table 3.1.

To calculate the DM annihilation induced positron differential flux at the location of the Earth, after propagation we follow [141, 148],

$$\frac{d\Phi_{e^+}}{dE} = \frac{c}{4\pi}f = \frac{c}{8\pi b(E,\vec{x})}\left(\frac{\rho(\vec{x})}{M_\chi}\right)^2 \sum_f \langle\sigma V\rangle_f \int_E^{M_\chi} dE_s \frac{dN^f_{e^+}}{dE}(E_s) I(E,E_s,\vec{x}), \quad (3.4)$$

Model	δ	$\mathcal{K}_0[kpc^2/Myr]$	$L[kpc]$
MIN	0.55	0.00595	1
MED	0.70	0.0112	4
MAX	0.46	0.0765	15

Table 3.1: Propagation parameters for positrons (adapted from [148]).

where $c = 3 \times 10^{10}$ cm.s^{-1} denotes the speed of light in vacuum, E_s denotes the source energy, and $I(E, E_s, \vec{x})$ denotes a halo function, which is a Green's function from a source with fixed energy E_s to any energy E. The halo function[1] is quite pivotal since it incorporates all the astrophysics and this is independent of any particle physics model [141].

3.2 Anti-protons Propagation

The propagation of anti-protons is governed by a diffusion equation analogous to that of positrons. The number density per unit energy is given by,

$$f(t, \vec{x}, K) = \frac{dN_{\bar{p}}}{dK}. \tag{3.5}$$

Similarly when imposing boundary conditions f drops to zero for $z = \pm L$ and $r = R$. $K = E - m_p$ yields the kinetic energy of the anti-protons. Since $m_p \gg m_e$ then the energy loss term can be neglected (this term was instead important for positrons) [141]. Following the formalism from [141], the diffusion equation for anti-protons is given by,

$$\frac{\partial f}{\partial t} - \mathcal{K}(K)\dot{\nabla}^2 f + \frac{\partial}{\partial z}\left(\mathrm{sign(z)} f V_{\mathrm{conv}}\right) = Q - 2h\delta(z)\left(\Gamma_{\mathrm{ann}} + \Gamma_{\mathrm{non-ann]}}\right) f, \tag{3.6}$$

where the pure diffusion term can again be expressed as $\mathcal{K}(K) = \mathcal{K}_0 \beta (p/\mathrm{GeV})^{\delta}$, for the anti-proton momentum $p = \sqrt{K^2 + 2m_p K}$ and anti-proton velocity $\beta = v_{\bar{p}}/c = \sqrt{\frac{1-m_p^2}{(K+m_p)^2}}$. $\mathcal{K}_0$ and δ values can be found in [141]. V_{conv} denotes the convective wind, which is assumed to be constant and is characterised by an orientation directed outward from the galactic plane. $h = 0.1$ kpc $\ll L$ denotes the galactic plane's thickness for the anihilation of $\bar{p}$ on interstellar protons. Table 3.2 summarizes the propagation parameters for anti-protons. Even in the anti-protons case, we utilize the values for L from table 3.1. The wind has the ability to push away anti-protons with energy $\lesssim 10\ m_p$.

[1]The numerical form values were found in http://www.marcocirelli.net/PPPC4DMID.html

$\Gamma_{ann} = \left(n_H + 4^{2/3} n_{He}\right) \sigma_{p\bar{p}}^{\rm ann} v_{\bar{p}}$ denotes the annihilation rate of $\bar{p}$ on interstellar protons within the galactic plane, where the hydrogen density is given by $n_H \approx 1/\text{cm}^3$, while the helium density is given by $n_{He} \approx 0.07 n_H$, the factor $4^{2/3}$ accounts for the difference in geometrical cross section and $\sigma_{p\bar{p}}^{\rm ann}$ is given by [146, 149],

$$\sigma_{p\bar{p}}^{\rm ann} = \begin{cases} 661\left(1 + 0.0115 K^{-0.774} - 0.984 K^{0.0151}\right) \text{mbarn}, & \text{for } K \leq 15 \text{ GeV} \\ 36 K^{-0.5} \text{ mbarn}, & \text{for } K \geq 15.5 \text{ GeV} \end{cases}. \tag{3.7}$$

$\Gamma_{\rm non-ann}$ denotes the interaction rate on interstellar protons within the galactic plane, where anti-protons do not annihilate but lose a significant amount of their energy. In essence these should be invoked in the flux, with a degraded energy. Conventionally, they are referred to as "tertiary anti-protons". However, here we instigate a rather simplifying approximation where they are removed from the flux. Both the annihilating and non-annihilating cross-sections contribute to the inelastic anti-proton cross-section given by,

$$\sigma_{p\bar{p}}^{\rm inel} = \sigma_{p\bar{p}}^{\rm ann} + \sigma_{p\bar{p}}^{\rm non-ann}. \tag{3.8}$$

The inelastic cross-section takes the form defined in [149],

$$\sigma_{p\bar{p}}^{\rm inel}(K) = 24.7\left(1 + 0.584 K^{-0.115} + 0.856 K^{-0.566}\right) \text{mbarn}. \tag{3.9}$$

Model	δ	$\mathcal{K}_0[kpc^2/Myr]$	$V_{\rm conv}[\text{km}/s]$
MIN	0.86	0.0016	13.5
MED	0.70	0.0112	12
MAX	0.46	0.0765	5

Table 3.2: Propagation parameters for anti-protons (adapted from [141]).

It is worth noting that, similar to positrons, the effects of re-acceleration are negligible, especially for our energies of interest[2]. Employing steady state boundary conditions to equation (3.6), the first term drops to zero and the diffusion equation can be solved analytically [147, 150, 151]. For the "no-tertiaries" approximation adopted here, DM annihilation induced anti-protons differential flux at the location of the Earth is given by [141],

$$\frac{d\Phi_{\bar{p}}}{dK} = \frac{v_{\bar{p}}}{8\pi}\left(\frac{\rho_\odot}{M_\chi}\right)^2 \mathcal{R}(K)\langle\sigma V\rangle \frac{dN_{\bar{p}}}{dK}, \tag{3.10}$$

[2] The energies of interest are energies above 75 GeV

where $v_{\bar{p}}$ is the speed of the anti-protons, $\rho_\odot$ is the DM density in the solar neighbourhood, $\frac{dN_{\bar{p}}}{dK}$ is the anti-protons yield function and $\mathcal{R}(K)$ encapsulate all the astrophysics of production and propagation of anti-protons and it is defined by,

$$\log\left(\frac{\mathcal{R}(K)}{\text{Myr}}\right) = a_0 + a_1\kappa + a_2\kappa^2 + a_3\kappa^3 + a_4\kappa^4 + a_5\kappa^5, \tag{3.11}$$

where $\kappa = \log_{10}\frac{K}{\text{GeV}}$ and we use a_i values for MIN, MED and MAX models from [141].

3.3 Gamma-rays Propagation

Unlike cosmic rays, gamma rays have a null charge so as a consequence they are not deflected as they propagate, hence they travel in straight lines from the galactic centre to the Earth. The gamma ray differential flux from a region $\Delta\Omega$ is given by [141],

$$\frac{d\Phi_\gamma}{dE}(E_\gamma) = \frac{r_\odot}{8\pi}\left(\frac{\rho_\odot}{M_\chi}\right)^2 \bar{J}\Delta\Omega\langle\sigma V\rangle\frac{dN_\gamma}{dE_\gamma}, \tag{3.12}$$

where $r_\odot$ is the distance from the galactic centre to the location of the Earth, $\bar{J}$ is the averaged J-factor over some region $\Delta\Omega$. $\frac{dN_\gamma}{dE_\gamma}$ is the gamma rays yield function.

The J-factor[3] in the DM annihilation case is given by,

$$J = \int_{\text{l.o.s}} \frac{ds}{r_\odot}\left(\frac{\rho(r(s,\theta))}{\rho_\odot}\right)^2, \tag{3.13}$$

where $r(s,\theta) = \left(r_\odot^2 + s^2 - r_\odot s\cos\theta\right)$ is centered on the galactic centre, θ denotes the aperture angle between the direction of the line of sight and the axis that connects the Earth to the GC, and s is a variable that runs along the line of sight. The J-factor is essential when one computes the flux of gamma rays from a given direction. However, more often, one needs to compute the integrated flux over a region $\Delta\Omega$[4]. Hence, the J-factor is replaced with the average J-factor for such a region, and it is defined as,

$$\bar{J}(\Delta\Omega) = \frac{\left(\int_{\Delta\Omega} J d\Omega\right)}{\Delta\Omega}. \tag{3.14}$$

[3] Interpolation forms are found in http://www.marcocirelli.net/PPPC4DMID.html.

[4] e.g. this commensurate to the window of observation or the resolution of the telescope.

In this work, we consider a region which is a disk characterised by an aperture angle $\theta_{\rm max}$ centred around the galactic centre,

$$\bar{J} = \frac{2\pi}{\Delta\Omega} \int d\theta \sin\theta J(\theta), \tag{3.15}$$

with

$$\Delta\Omega = \int_0^{\theta_{\rm max}} d\theta \sin\theta. \tag{3.16}$$

In order to get $\bar{J}$ values we use values from Table 3 presented in [141].

Chapter 4

Parameter Space for AMS-02 and Fermi-LAT Excesses

In this section we produce the parameter spaces for the AMS-02 and Fermi-LAT excesses, this is achieved through the formalism established in chapter 3 for the Madala hypothesis. We will consider both the $2 \to 2$ and $2 \to 3$ scattering processes.

4.1 Positron Excesses

In standard cosmic ray paradigms, positrons are induced through an inelastic scattering of primary cosmic rays on the interstellar medium's hydrogen. The indirect detector HEAT [111] reported excesses in positrons, later on in 2008 PAMELA confirmed the excesses through the observation of the electron-to-positron ratio excess above ~ 10 GeV [152]. Recently, a more sensitive detector AMS-02 made more precise measurements of positrons up to 1 TeV and confirmed excesses above 25.2 GeV [22]. In Fig. 4.1 an excess materializes above 25.2 ± 1.8 GeV, this is established at a significance transcending 6σ. For clarity in Fig. 4.1, E_0 denotes the transition energy, and to determine E_0 for the spectral index γ that starts to increase, a double-law approximation (corresponds to Eq. (3) in Ref. [22]) is employed,

$$\Phi_{e^+} = \begin{cases} C(E/55.58 \text{ GeV})^{\gamma}, & E \leq E_0 \\ C(E/55.58 \text{ GeV})^{\gamma}(E/E_0)^{\Delta\gamma}, & E > E_0 \end{cases}. \tag{4.1}$$

C denotes the normalization flux constant. The source of the excesses is still unknown, however, some studies suggest that primary positron sources beyond the conventional cosmic ray model are necessary to explain the positron excesses data [153]. Currently, there exist three alternatives in literature to explain these detections, namely: contribution from pulsars, ordinary cosmic rays from supernova remnants, and DM annihilation/decay.

Pulsars are highly magnetized and rapidly rotating neutron stars. They are also known as powerful sources in the galaxy with the potential to produce primary electrons/positrons at high energies [115, 154]. In essence electrons/positrons get torn away from the surface of the neutron star by the intense electric field generated by the strong spinning magnetic field. The charged particles are accelerated by the strong magnetosphere of the pulsar and induce an electromagnetic cascade through the emission of curvature radiation[1], subsequently, positron/electron pairs can be produced [155, 156]. The pulsar will induce a relativistic wind which impacts the much slower supernova ejecta to create a reverse shock (termination shock) that propagates backward, towards the pulsar [157]. A bubble of relativistic hot magnetized plasma called pulsar wind nebulae (PWN) is created within a region bound by wind termination shock on one side and the ejecta on the other side [158]. It is worth noting that the incoming induced pairs are accelerated to higher energies within the termination shock region. Subsequently, after undergoing acceleration these particles gather in the PWN, then eventually get released into the interstellar medium at the disruption of this PWN's magnetic field. Authors from [159] argue that mature pulsars can be treated as burst-like sources of e^-/e^+ if it is assumed that the injection mechanism is fast and the subsequent pulsar's residual energy is negligible. Studies such as Ref. [160] have demonstrated that by applying pulsar models to explain the reported positron excess, it is very likely that pulsars are responsible for more, if not the entirety, of the detected positron excess.
As mentioned previous in section 1.5.3 DM can also explain the positron excesses. In a multitude of scenarios DM can either account completely or partially for the positron excesses [161, 162]. In this work we consider the DM contribution along with both the pulsar and secondary positron contributions. The overall flux contribution is given by,

$$\Phi_{e^+}(\mathrm{E}) = \Phi_{e^+}^{\mathrm{DM}}(\mathrm{E}) + \Phi_{e^+}^{\mathrm{Pulsar}}(\mathrm{E}) + \Phi_{e^+}^{\mathrm{Sec}}(\mathrm{E}), \tag{4.2}$$

where $\Phi_{e^+}^{\mathrm{Sec}}(\mathrm{E})$ accounts for secondary positrons induced by collisions between cosmic rays and interstellar gas (hydrogen) at low energies. Here we adapted $\Phi_{e^+}^{\mathrm{Sec}}(\mathrm{E})$ from [22],

[1] Curvature radiation refers to the electromagnetic radiation from relativistic charged particles when they move along the curved field lines.

$$\Phi_{e^+}^{\text{Sec}}(\text{E}) = \left(\frac{\text{E}}{\hat{E}}\right)^2 \text{C}_d \left(\frac{\hat{\text{E}}}{\text{E}_1}\right)^{\gamma_d}, \tag{4.3}$$

where C_d denotes the normalization factor and γ_d denotes the spectral index. We employ force-field approximation to account for solar-modulations effects, with the energy of the particles in interstellar space,

$$\hat{\text{E}} = \text{E} + \phi_{e^+}, \tag{4.4}$$

where ϕ_{e^+} denotes the effective solar potential that accounts for solar effects[2]. According to Ref. [22], in order to minimize the correlation between C_d and γ_d, E_1 is taken to be about 7.0 GeV. Using the supplemented material from [22], $\gamma_d = -4.07 \pm 0.06$, $\phi_{e^+} = 1.10 \pm 0.03$ GeV and $\text{C}_d = (6.51 \pm 0.14) \times 10^{-2}$ $[\text{m}^2\,\text{sr}\,\text{s}\,\text{GeV}]^{-1}$. For $\Phi_{e^+}^{\text{Pulsar}}(\text{E})$, we employ a pulsar background model from [164] for B1055-52. B1055-52 is used because it can account for the high-energy positron spectrum. Conventionally, Geminga is a more attractive source of the positron excesses but as suggested in [164], the source is disfavoured by the constraints obtained from Fermi-LAT γ-ray observations. Finally $\Phi_{e^+}^{\text{DM}}(\text{E})$ is calculated by equation (3.4). It is worth highlighting that since we are working in a model-dependent way, we use $\frac{dN_{e^+}^f}{dE}$ from the Madala hypothesis [1].

4.2 Anti-protons Excesses

Another diagnostic tool to probe and constrain DM models is the anti-protons flux from the galactic centre. For the past years, PAMELA and AMS-02 have been working hard to measure anti-proton flux and anti-proton-to-proton ratio with precision. In essence, the anti-protons are produced by a collision between the cosmic ray protons (and Helium) and the interstellar medium. The induced anti-protons propagate in random walks just like positrons, though it is worth noting that the propagation contributes largely to uncertainties whenever predicting astrophysical background and DM annihilation anti-proton signal [165]. A multitude of formalisms invokes the Boron-to-Carbon (B/C) ratio to constrain the propagation parameters [166, 167]. Recently, the AMS-02 [23] reported anti-proton flux and anti-proton-to-proton

[2]Solar modulation of positrons emerges from cosmic rays encountering a turbulent solar wind (characterized by an embedded heliospheric magnetic field) when entering the heliosphere [163]. As a result, there is a significant global and temporal variations in both the intensity and energy of cosmic rays as a function of the position inside the heliosphere.

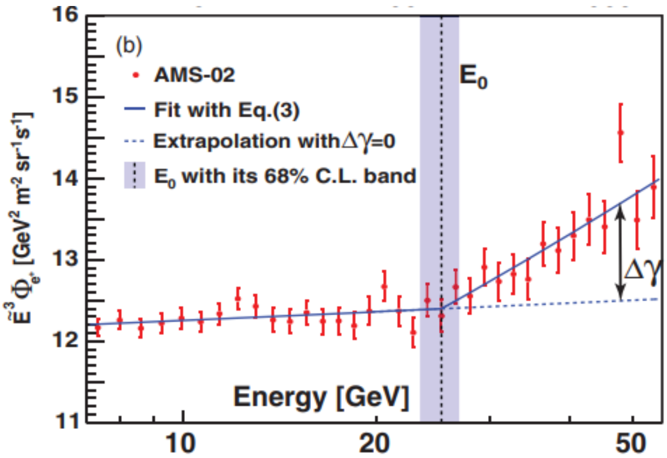

Figure 4.1: Double power law fit to the positron flux in the energy range $7.10-55.8$ GeV. The measured positron flux values are denoted by red data points. $E_0 = 25.2 \pm 1.8$ GeV, and the dashed blue lines and bands show the value of E_0 along with its associated error where changes in the spectral index occurs. Adapted from [22].

ratio with great precision up to an absolute rigidity of 450 GV. The aforementioned revelation suggests an excess of anti-protons over the expected astrophysical background. Most familiar paradigms accommodate these excesses through DM annihilation/decay [168]. In the nutshell the AMS-02 flux data within astrophysical uncertainties, the predicted secondary anti-proton flux still tends to be smaller than the observed flux at higher energies, this suggests a contribution from DM for this energy range [169]. Some DM models can account for anti-proton excess independently of constraints from other observations such as gamma-rays [170, 171]. Authors from [172] argue that the anti-proton excess can be robustly explained by DM annihilation via b-quarks of a $40-70$ GeV WIMP with a possibility of heavier masses. In this case, the overall predicted flux is given by,

$$\Phi_{\bar{p}}(\mathrm{E}) = \Phi_{\bar{p}}^{\mathrm{DM}}(\mathrm{E}) + \Phi_{\bar{p}}^{\mathrm{Backg}}(\mathrm{E}), \tag{4.5}$$

where $\Phi_{\bar{p}}^{\mathrm{DM}}(\mathrm{E})$ is given by equation (1.10) and $\Phi_{\bar{p}}^{\mathrm{Backg}}(\mathrm{E})$ is calculated by the background model from [173]. The background model considers correlations in the systematic errors that can potentially mimic a DM signal. Taking the aforementioned into consideration reduces the anti-proton excesses. Even here we employ $\frac{dN_{\bar{p}}}{dK}$ from Madala hypothesis [1].

4.3 Fermi-LAT Excess

Several years ago an excess of gamma-rays was been reported at a few GeV energies, in a narrow region around the Galactic Centre. In brief terms, the inner region of the Galactic Centre is found to be brighter than the expected diffuse gamma-ray emission from conventional models and catalogs of known gamma-ray sources. This is an intriguing anomaly since the statistical significance of the excess is gradually augmented with more data from Fermi-LAT. Another factor to note is the good agreement between the angular distribution and expectations from DM annihilation. One attractive paradigm of explaining the gamma-ray excess is through DM models [174–178]. [179,180] elucidated that a DM mass (for WIMPs) of $\approx$ 10 GeV can explain the excess data when DM annihilate into lepton/anti-lepton pairs but the pure $b\bar{b}$ final states provide the best fit for DM mass between 30 to 40 GeV. Other possible explanations of the excess have surfaced, these include a central point source [181], pions from the collision of cosmic rays with gas [176, 181], a burst injection of electrons [182] and a population of millisecond pulsar [178, 180, 183]. It is pointed out in [184] that millisecond pulsar's spectral shape for sub-GeV energies is too soft when compared with the observed spectrum of the GeV excess, and the millisecond pulsars can only account for $\approx$ 10% of the gamma-ray excess. There exist several groups that refute the existence of the gamma-ray excess and they justify this through the consideration of the uncertainties in the modeling of sources and interstellar emission [181]. Authors from [185] probed both the foreground and background models' uncertainties and inferred that indeed an excess materializes, though the interstellar emission model uncertainties are too big to prove a DM origin. Nevertheless, a DM interpretation of this gamma-ray excess is still plausible. Recently, [186] argues that through robust uncertainty modeling of the interstellar emission models, a DM interpretation of the excess is still possible. In this case, the contribution from DM is dominant, so the overall predicted flux is given by equation (3.12). We employ the gamma-ray yield functions from the Madala hypothesis [1].

4.4 Parameter Spaces

As mentioned earlier (see section 2.4) only spin 0 DM is considered for both the $2 \to 2$ and $2 \to 3$ scattering processes. The DM mass ranges between 75 GeV to 1000 GeV for $2 \to 2$ scattering and 200 GeV to 1000 GeV for $2 \to 3$ scattering, the mass ranges are characterised by 100 GeV spacing. These DM mass ranges are used since the degree of freedom for our DM

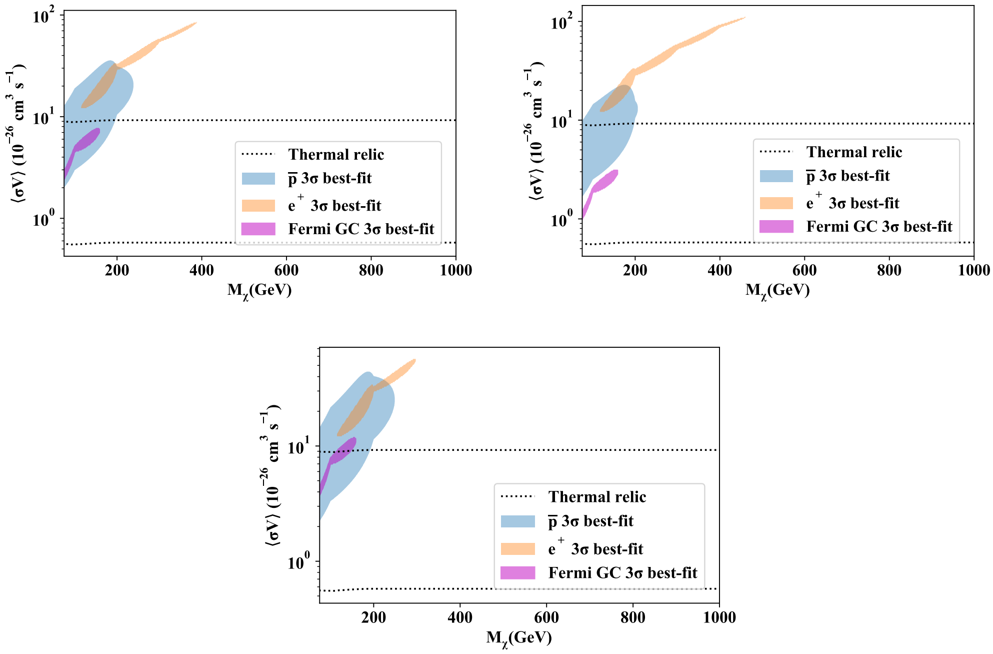

Figure 4.2: The parameter space fitting the $2 \to 2$ scattering to the Fermi-LAT galactic centre excess, AMS-02 anti-proton and positron spectra. The shaded regions represent the 3σ confidence interval. The region between the thermal relic lines represents the uncertainties in local DM density and galactic halo profile. This plot assumes the MED diffusion scenario. Top left: Einasto profile for the Milky-Way halo from Ref. [53]. Top right: contracted Einasto profile for the Milky-Way halo from Ref. [141]. Bottom: NFW profile for the Milky-Way halo from Ref. [49].

candidate is, as yet, unconstrained by the LHC data. Consequently, a wide parameter space is scanned, from the lowest DM masses that can induce real S bosons up to 1 TeV. In the $2 \to 3$ scattering, the lower mass limit is that required to produce H and h bosons together. The aforementioned serve as a cornerstone to constrain the allowed DM parameter space (in the M_χ and $\langle \sigma V \rangle$ plane) using both the AMS-02 and Fermi-LAT data. The induced allowed parameter space will lay a foundation for calculating predictions for MeerKAT and radio observations of dwarf spheroidal galaxies. The recipe for constraining the allowed parameter space lies in the comparison between the predicted cosmic-ray fluxes at Earth and the AMS-02 data [22, 23].

To strengthen the parameter space we also compare the predicted gamma-ray fluxes with the Fermi-LAT galactic centre excess data [24]. The region of interest for the gamma-ray case is 10° around the galactic centre. We acknowledge that the Fermi-LAT galactic centre excesses suffer from uncertainties due to systematics [24]. In all cases, we employ Milky-Way halo models described in section 1.4. In Fig. 4.2 we fit the Madala hypothesis DM fluxes to the AMS-02 and Fermi-LAT excesses for $2 \to 2$, to produce the best-fit parameter space for MED diffusion scenario [141] and for the Einasto, contracted Einasto and NFW halo profiles. The thermal relic cross-section [187] is denoted as a band to account for systematic uncertainties in the Milky-Way's DM density and halo profile. The uncertainties are established from $\rho_\odot$'s estimates (for instance, we refer the reader to [188] and [189]). The same was done in Fig. 4.3 but the difference is the scattering process ($2 \to 3$). As depicted in Fig. 4.2, regions for masses M_χ below 200 GeV in the parameter space are slightly above the thermal relic value. Furthermore, we observe that for M_χ below 200 GeV the three excess regions cluster together even though a complete overlap of all regions is not perceptible. This may be attributed to the unresolved systematic issues in the excess data. There is a larger amplitude of the positron flux and even with the inclusion of the pulsar background model [164], this suggests there is still some room left for a large DM contribution. However, the gamma ray excess data [24] is very well studied with robust background models, hence, they can only accommodate much smaller DM contributions. In principle, the AMS-02 positron data is more sensitive to the systematic issues simply because so little is known about the positron background, this hints that they may be missing ingredients in the astrophysical modelling. As things stand, the positron data may be a bit unreliable in constraining the parameter space of our model. Nevertheless, we obtain the best case when MED diffusion scenario and Einasto (or NFW) halo profile are employed. With regards to the preferred halo profile, this is somewhat a deviation from what DM model-independent searches suggest (see e.g [186]), where a contracted DM halo profile is preferred to account

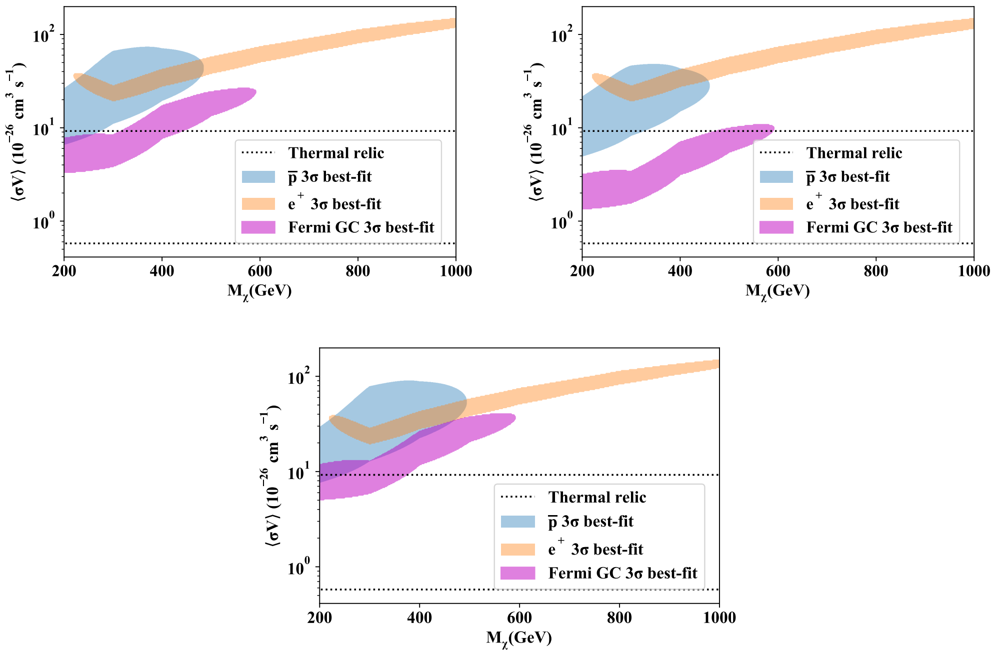

Figure 4.3: The parameter space fitting the $2 \to 3$ scattering to the Fermi-LAT galactic centre excess, AMS-02 anti-proton and positron spectra. The contours are 3σ confidence intervals on the M_χ and $\langle \sigma V \rangle$ plane. The thermal relic [187] is denoted as a band to account for uncertainties in the local DM density and galactic halo profile. This plot assumes the MED diffusion scenario. Top left: Einasto profile for the Milky-Way halo from Ref. [53]. Top right: contracted Einasto profile for the Milky-Way halo from Ref. [141]. Bottom: NFW profile for the Milky-Way halo from Ref. [49].

for DM interpretation of the galactic centre excess spectrum from [24].

In Fig. 4.3 we observe that $2 \to 3$ scattering process is characterised by a far less constraining power for the three excesses. It is apparent from Fig. 4.3 that the $2 \to 3$ case produces the least overlap of the three best-fits for both the Einasto and contracted halo profile. However, for the NFW halo profile just slightly above the relic band, we observe a potential mutual overlap of the three best-fits at DM mass $400 - 450$ GeV. The parameter spaces' sensitivity to the choice of halo profile is in contrast with Ref. [190], where a choice of halo profile provides a negligible impact on the DM limits.
More interestingly, from Fig. 4.4 it is apparent that the MAX diffusion scenario for the $2 \to 3$ scattering process and NFW halo profile produces an overlap between the best-fits of the three excesses. However, we do acknowl-

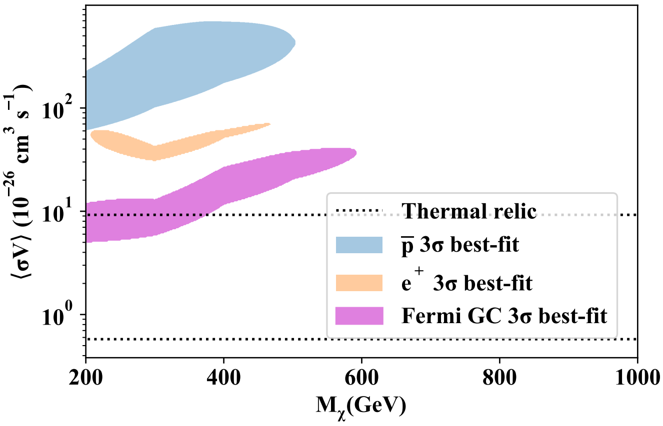

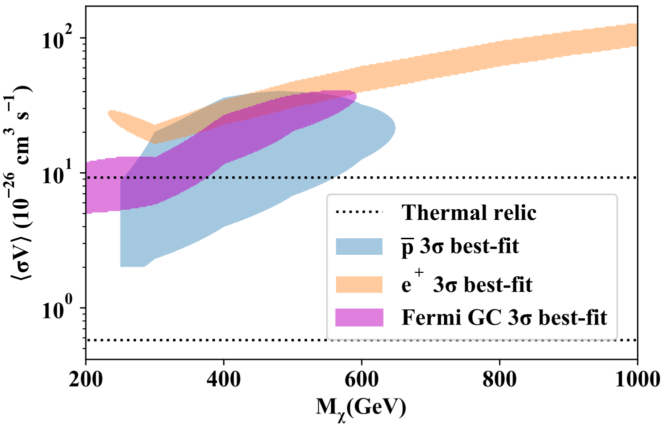

Figure 4.4: The parameter space fitting the $2 \rightarrow 3$ scattering to the Fermi-LAT galactic centre excess, AMS-02 anti-proton and positron spectra. The contours are 3σ confidence intervals on the M_χ and $\langle \sigma V \rangle$ plane. The thermal relic [187] is denoted as a band to account for uncertainties in the local DM density and galactic halo profile. Top: We have the MIN diffusion scenario. Bottom: We have the MAX diffusion scenario. This is for the NFW halo profile from Ref. [49].

edge that the overlap materializes slightly above the thermal relic cross section band. Furthermore, in Fig. 4.4 the results for MIN diffusion scenario demonstrate no best-fits overlap between the three excesses.

Chapter 5

Radio Emission from Dark Matter Halos

This chapter explores the synchrotron emission predictions for different DM halo environments. Firstly, the predictions are compared to the sensitivity of the MeerKAT in the L-band along with the full-SKA. The results from the comparison demonstrate that MeerKAT is currently at the forefront (has a highly competitive constraining power) of indirect DM search since its limits are vastly higher than those of the Fermi-LAT data. Secondly, the synchrotron emission predictions are compared with the existing radio data to produce exclusion limits, and the revelation is that the limits do not rule out the Madala hypothesis.

5.1 Formalism for Synchrotron Emission from Dark Matter Halos

Since the regime of interest in this work is the radio band, in this section we consider synchrotron emission from Madala DM induced positrons. The average power per positron with energy E is given by [191],

$$P_{\text{synch}}(\nu, E, r, z) = \int_0^\pi \frac{\sin^2\theta}{2} 2\pi\sqrt{3} r_e m_e c \nu_g F_{\text{synch}}\left(\frac{\kappa}{\sin\theta}\right) d\theta \ , \tag{5.1}$$

where ν denotes the observed frequency, r denotes the position within the halo, z denotes the redshift of the source of interest, r_e denotes the electron's classical radius, m_e denotes the electron's mass, c is the speed of light in vacuum, and finally, ν_g denotes the gyro-frequency for the non-relativistic case. Then the parameter κ is further defined by,

$$\kappa = \frac{2\nu(1+z)}{3\nu_g\gamma^2}\left(1+\left(\frac{\gamma\nu_p}{\nu(1+z)}\right)^2\right)^{\frac{3}{2}} , \tag{5.2}$$

with the ν_p denoting the plasma frequency which turns out to be directly proportional to $\sqrt{n_e}$ (where n_e denotes the thermal electron density), and γ denotes the Lorentz factor of the positron. Additionally, the synchrotron kernel is given by,

$$F_{\text{synch}}(x) = x\int_x^\infty K_{5/3}(y)dy \approx 1.25x^{\frac{1}{3}}e^{-x}\left(648+x^2\right)^{\frac{1}{12}} , \tag{5.3}$$

where $K_{5/3}$ is the modified Bessel function of 5/3 order. Then the emissivity of synchrotron radiation is given by,

$$j_{\text{synch}}(\nu, r, z) = \int_{m_e}^{M_\chi}\left(\frac{dn_{e^-}}{dE}+\frac{dn_{e^+}}{dE}\right)P_{\text{synch}}(\nu, E, r, z)dE , \tag{5.4}$$

where $\frac{dn_{e+}}{dE}$ and $\frac{dn_{e-}}{dE}$ are positron and electron equilibrium distributions respectively (see below for their explanation). By integrating over the volume of interest then we have the flux density spectrum within the halo radius r given by,

$$S_{\text{synch}}(\nu, z) = \int_0^r \frac{j_{\text{synch}}(\nu, r', z)}{4\pi D_L^2}d^3r' , \tag{5.5}$$

where D_L denotes the luminosity distance to the DM halo of interest.
To account for diffusion and energy loss of electrons/positrons from DM annihilation, for an assumption where the processes of reacceleration and convection are negligible, the diffusion-loss equation is given by,

$$\frac{\partial}{\partial t}\frac{dn_e}{dE} = \nabla\left(D(E,\mathbf{x})\nabla\frac{dn_e}{dE}\right)+\frac{\partial}{\partial E}\left(b(E,\mathbf{x})\frac{dn_e}{dE}\right)+Q_e(E,\mathbf{x}) , \tag{5.6}$$

where $D(E,\mathbf{x})$ denotes the spatial diffusion function and $b(E,\mathbf{x})$ denotes the energy loss rate. The spatial diffusion is given by [192],

$$D(E) = D_0\left(\frac{d_0}{1\text{kpc}}\right)^{\frac{2}{3}}\left(\frac{\bar{B}}{1\mu G}\right)^{-\frac{1}{3}}\left(\frac{E}{\text{GeV}}\right)^{\frac{1}{3}} , \tag{5.7}$$

where the diffusion constant $D_0 = 3.1\times10^{28}$ cm^{2}s^{-1}, $\bar{B}$ denotes the average magnetic field and d_0 denotes the smallest scale where the magnetic field is found to be homogenous. The energy loss rate is given by [118],

$$b(E) = b_{\text{IC}}E^2\left[1+z\right]^4+b_{\text{synch}}E^2\bar{B}^2+b_{\text{coul}}\bar{n}\left[1+\frac{1}{75}\log\left(\frac{\gamma}{\bar{n}}\right)\right]+b_{\text{brem}}\bar{n}\left[\log\left(\frac{\gamma}{\bar{n}}\right)+0.36\right] , \tag{5.8}$$

Where $\bar{n}$ denotes the average electron density, $\gamma = \frac{E}{m_e c^2}$ denotes the electron Lorentz factor, while $b_{\rm IC}$, $b_{\rm synch}$, $b_{\rm Coul}$ and $b_{\rm brem}$ are inverse-Compton, synchrotron, Coulomb and bremsstrahlung energy loss factor. These take values 0.25, 0.0254, 6.13 and 1.51 in units 10^{-16} GeVs^{-1} respectively. It is worth highlighting that both the diffusion and energy loss terms are written using the average values of the magnetic field and the thermal density, such that they can be assumed to have no spatial dependence.

For the the case of spherical symmetry and limits whereby diffusion is negligible Eq. (5.6) takes the form,

$$\frac{dn_e}{dE} = \frac{1}{b(E)} \int_E^{M_\chi} dE' \, Q_e(r, E') \; . \tag{5.9}$$

But in general the solution requires a Green's function,

$$\frac{dn_e}{dE}(r, E) = \frac{1}{b(E)} \int_E^{M_\chi} dE' \, G(r, E, E') Q_e(r, E') \; , \tag{5.10}$$

where the Green's function is defined by,

$$\begin{aligned} G(r, E, E') = & \frac{1}{\sqrt{4\pi\Delta v}} \sum_{n=-\infty}^{\infty} (-1)^n \int_0^{r_h} dr' \, \frac{r'}{r_n} \\ & \times \left(\exp\left(-\frac{(r' - r_n)^2}{4\Delta v} \right) - \exp\left(-\frac{(r' + r_n)^2}{4\Delta v} \right) \right) \\ & \times \frac{Q_e(r')}{Q_e(r)} \; , \end{aligned} \tag{5.11}$$

where the index n denotes a set of image charges with $r_n = (-1)^n r + 2 n r_h$ and r_h conventionally denotes the maximum considered diffusion radius, however, we use twice the halo virial radius for our case. Lastly, Δv is given by

$$\Delta v = v(u(E)) - v(u(E')) \; , \tag{5.12}$$

with

$$\begin{aligned} v(u(E)) &= \int_{u_{min}}^{u(E)} dx \; D(x) \; , \\ u(E) &= \int_E^{E_{max}} \frac{dx}{b(x)} \; . \end{aligned} \tag{5.13}$$

5.2 Synchrotron Emission from Dark Matter Halo Environments

In section, we gauge whether any existing radio data can effectively limit our parameter space. The parameter space that best fits the AMS-02 and Fermi-LAT excesses are used to make DM synchrotron radio emission for sources, M31, Coma, and Ophiuchus. Subsequently, these DM radio predictions are compared to the radio data in M31 as well as the Coma and Ophiuchus galaxy clusters to induce 3σ level exclusion limits. To achieve the aforementioned we need to pay more attention to the DM halo environments governing the sources under consideration.

5.2.1 M31 Halo Environment

M31 (or Andromeda) is the closest independent galaxy to our own. DM annihilation induced $e^{\pm}$ within the DM halo emits synchrotron emission on the radio frequencies due to M31's magnetic field. Naturally, one will expect high radio fluxes from M31, solely because of the size of the galaxy and its DM halo, magnetic field's strength, and nearby distance. For M31 we assume halo data from Ref. [193] at a distance of 770 kpc. For the DM density distribution, we employ NFW density profile (given by Eq. (1.20)), since previous studies [193, 194] have demonstrated that rotation curve data in M31 can be optimally fit using NFW density profile. The virial mass takes the value of $1.04 \times 10^{12}\mathrm{M}_{\odot}$. For the magnetic field profile, we employ [195],

$$B(r) = \frac{4.6 r_1 + 64}{r_1 + r}\ \mu\mathrm{G}, \tag{5.14}$$

where $r_1 = 200$ kpc according to fittings in Ref. [195]. r_1 and r have the same dimensions (kpc in this case).For 14 kpc the magnetic field strength is given by $B = 4.6 \pm 1.2\ \mu$G. The thermal electron density distribution takes an exponential profile from Ref. [195],

$$n_e(r) = n_0 \exp\left(-\frac{r}{r_d}\right), \tag{5.15}$$

where central density is given by $n_0 = 0.06\ \mathrm{cm}^{-3}$ [196] and the disk scale radius is $r_d \approx 5$ kpc according to fittings in Ref. [195]. According to [197] spatial diffusion of secondary electrons is negligible for the magnetic field environment, since its time scale takes longer than that for energy losses. We predict multi-frequency emission fluxes for frequencies between $50 - 10^9$ MHz for M31. However, we only focus on the radio emission fluxes between

$50-10^4$ MHz. Subsequently, this is compared to the low frequency 408 MHz point flux [198] for a rather optimistic region of interest (50 arcminutes). It is worth noting that the optimistic region of interest was chosen to be compatible with the maximum resolvable scale for the instrument (Northern Cross) from [198].

5.2.2 Coma Halo Environment

For the Coma cluster DM halo we employ models from Ref. [192]. For the Coma cluster the virial mass is $1.33 \times 10^{15} M_{\odot}$ and virial concentration[1] $c_{\rm vir} = 10$, at the redshift $z = 0.0231$. Similar to M31 we use NFW density profile for Coma. For the thermal electron density distribution in Coma we follow [199, 200],

$$n_e(r) = n_0 \left(1 + \left[\frac{r}{r_s}\right]^2\right)^{-q_e} , \tag{5.16}$$

where $n_0 = 3.49 \times 10^{-3}$ cm^{-3} and $q_e = 0.981$. The magnetic field profile in Coma is given by [201],

$$B(r) = B_0 \left(\frac{n_e(r)}{n_0}\right)^{q_b} , \tag{5.17}$$

where $B_0 = 4.7$ μG and $q_b = 0.5$. The fittings from [201] suggest a magnetic field with a Kolmogorov power spectrum characterised by a minimal coherence length $\Lambda_{min} \approx 2$ kpc. For a region of interest of about 30 arcminutes, the Coma radio fluxes data from [202] with a frequency range $30.9 - 4850$ MHz was compared with the predicted radio fluxes.

5.2.3 Ophiuchus Halo Environment

For the Ophiuchus cluster we assume halo data from [203]. The virial mass is $1.1 \times 10^{15} M_{\odot}$ and virial radius is given by $r_{\rm vir} = 2.1$ Mpc at the redshift $z = 0.0296$. Even here we will employ the NFW density profile. In terms of the magnetic field and the thermal electron density distribution we adhere to the formalism in [204] which assumes that Ophiuchus follows profiles similar to that in Coma, where $B_0 = 5.225$ μG, $q_b = 0.74$, $n_0 = 0.29614$ cm^{-3} and $q_e = 0.412725$. Subsequently, predicted emissions are compared to the 153, 240 and 1477 MHz, radio fluxes from [205] for a region of interest of about 7 arcminutes.

[1]Relates the value of r_{-2} (the radius at which the effective logarithmic slope of the halo profile is -2) to the virial radius $r_{\rm vir}$ via $c_{\rm vir} = \frac{r_{\rm vir}}{r_{-2}}$.

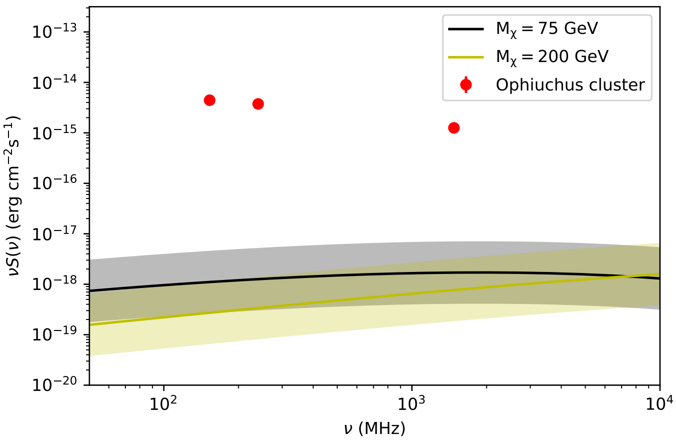

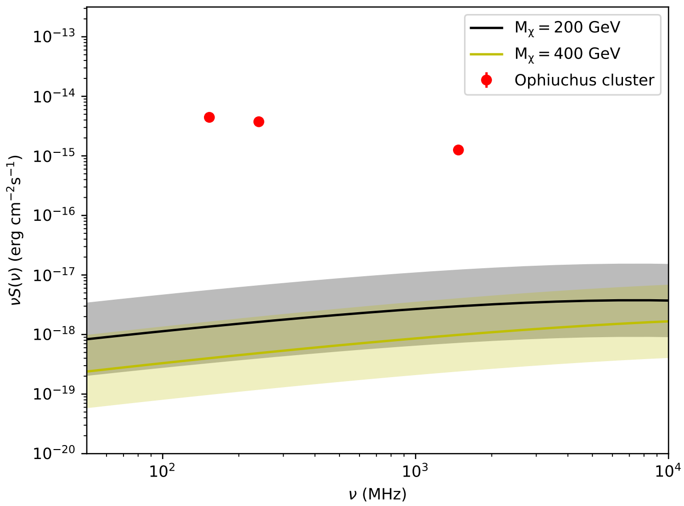

Figure 5.1: Synchrotron radio spectrum prediction compared to the observed radio data for Ophiuchus cluster. Top: We have $2 \to 2$ scattering. Bottom: we have $2 \to 3$ scattering.

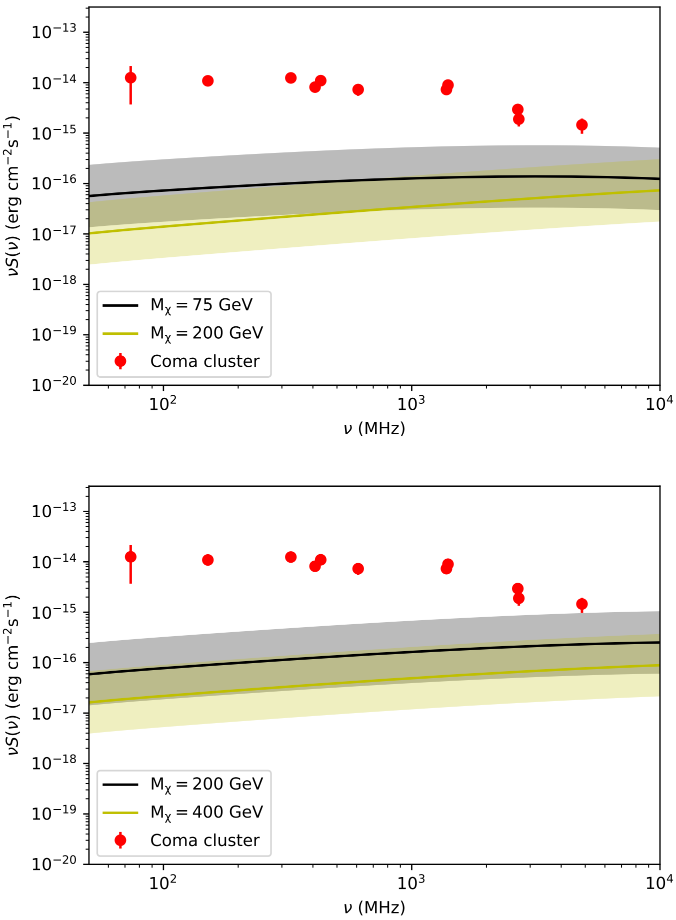

Figure 5.2: Synchrotron radio spectrum prediction compared to the observed radio data for Coma cluster. Top: We have $2 \rightarrow 2$ scattering. Bottom: we have $2 \rightarrow 3$ scattering.

5.2.4 Synchrotron Emission Versus Available Radio Data

We employ the DM halo environments described above along with the parameter space that best-fits the cosmic-ray and gamma-ray excesses (as shown in section 4.4) for both $2 \to 2$ and $2 \to 3$ cases. In section 4.4 we observed a closer clustering of the three excesses for masses below 200 GeV, hence, we employ smaller masses for our predictions. Furthermore, we assume that $\langle \sigma V \rangle_{22} \approx 10^{-25}$ cm^3 s^{-1} from the produced $2 \to 2$ parameter space, since this is the value where the closer clustering of the excesses occur. Similarly, for the $2 \to 3$ parameter space we observe a closer clustering for masses below 450 GeV and we assume that $\langle \sigma V \rangle_{23} \approx 2.5 \times 10^{-25}$ cm^3 s^{-1}. These parameter spaces give annihilating DM through the Madala hypothesis to induce highly energetic positrons/electrons, which in the presence of a magnetic field emits synchrotron emission in M31, Coma, and Ophiuchus. Through the recipe described in Section 5.1, synchrotron emission predictions were made. Subsequently, the predicted radio fluxes are compared to Coma [202] and Ophiuchus [205] radio observation data. We only considered the Coma and Ophiuchus clusters since they have more than one frequency data point available. In Fig. 5.1, it is evident that for the Ophiuchus cluster, $2 \to 3$ scattering offer slightly stronger emissions than $2 \to 2$ scattering. However, for both $2 \to 2$ and $2 \to 3$ cases, the observed radio data points are at least 5 orders of magnitude above the predicted synchrotron spectrum. Indeed, the predicted spectrum can only exceed the Ophiuchus radio data if we have a cross-section that is 10^5 times higher than the assumed cross-section ($\mathcal{O}(10^{-25}$cm^3 s$^{-}1))$ for our model. Coma cluster results are displayed in Fig. 5.2. Also, for the Coma cluster, the cross-section would have to be 10^4 times higher than the assumed cross-section ($\mathcal{O}(10^{-25}$cm^3 s$^{-}1))$ to exceed the Coma cluster radio data. The Coma cluster radio constraints are superior by a factor of 10 when compared to the ones for the Ophiuchus cluster.

5.2.5 Exclusion Limits

In order to corroborate the analysis above, the 3σ exclusion limits are produced through the comparison between the predicted synchrotron emission fluxes and M31 [198], Coma [202] and Ophiuchus [205] radio observation data. The M31 radio data used here have been highly constraining in other DM models (see e.g [206, 207]). In Fig. 5.3 (for both Einasto and NFW halo), we observe that M31 has better constraining limits transcending those of Coma and Ophiuchus. Yet again, it is evident that the Coma cluster limits are superior to those of the Ophiuchus cluster. Significantly, all the exclusion limits do not exclude our Madala DM model. With the radio DM-search regime entering a new era of high sensitivity and resolution, this will aid to place more stringent limits on the Madala hypothesis in near future.

5.3 MeerKAT Predictions for Reticulum II

Dwarf spheroidal galaxies are deemed pivotal in the DM community since they provide promising testing avenues for DM models [208]. They are considered as the closest galaxies other than the Milky Way and highly DM dominated objects in the local universe. One example of such an object is Reticulum II, and its discovery was found in the first year Dark Energy Survey data in 2015 [64, 209]. From spectroscopic studies performed in Ref. [210, 211] it can be inferred that Reticulum II is an ultra-faint galaxy and a satellite of the Milky Way. In this work we use Reticulum II for MeerKAT predictions, because of its ideal location [2] for southern hemisphere observation and a high J-factor [212–214]. According to Ref. [215, 216] dwarf galaxies favor a cored density profile. In this work, we employ two different cored density profiles. Firstly, we have the Einasto halo profile given by Eq. (1.21), where $\alpha = 0.4$, $r_s = 0.2$ kpc, and $\rho_s = 7 \times 10^7$ $M_\odot$ kpc^{-3} according to Ref. [121]. Secondly, we have the Burkert halo profile given by Eq. (1.22), and is characterized by set parameters $r_s = 0.23$ kpc, and $\rho_s = 4.1 \times 10^8$ $M_\odot$ kpc^{-3}. The J-factor is taken as 2×10^{19} GeV^2 cm^{-5}. For the magnetic field profile we follow Ref. [121],

$$B(r) = B_0 \exp\left(-\frac{r}{r_d}\right) , \tag{5.18}$$

where we assume $B_0 \approx 1$ μG, and the stellar-half-light radius r_d is about 35 pc [64, 209]. The thermal electron distribution follows an exponential profile (given by Eq. (5.15)) according to Ref. [121], where we assume $n_0 = 10^{-6}$ cm^{-3}. Even here, we assume that $\langle \sigma V \rangle_{22} \approx 10^{-25}$ cm^3 s^{-1} and $\langle \sigma V \rangle_{23} \approx 2.5 \times 10^{-25}$ cm^3 s^{-1}. When making synchrotron emission predictions, we include a shaded uncertainty band in our plots, this includes the uncertainties on the value of the cross-section (a consequence of the uncertainties on the value of $\rho_\odot$), the J-factor, and the magnetic field of the halo. To align with our assumption of arcminute scale emission when determining the sensitivity, the region of flux integration is taken as 3 arcminutes.

In Fig. 5.4 we observe that only the lower masses are detectable at the 5σ confidence interval with MeerKAT (with an observation of just 100 hours). Furthermore, we do not observe the coverage of the entire uncertainty band

[2] Reticulum II is located well below the galactic plane at about 30 kpc, where there is low and uniform Galactic foreground.

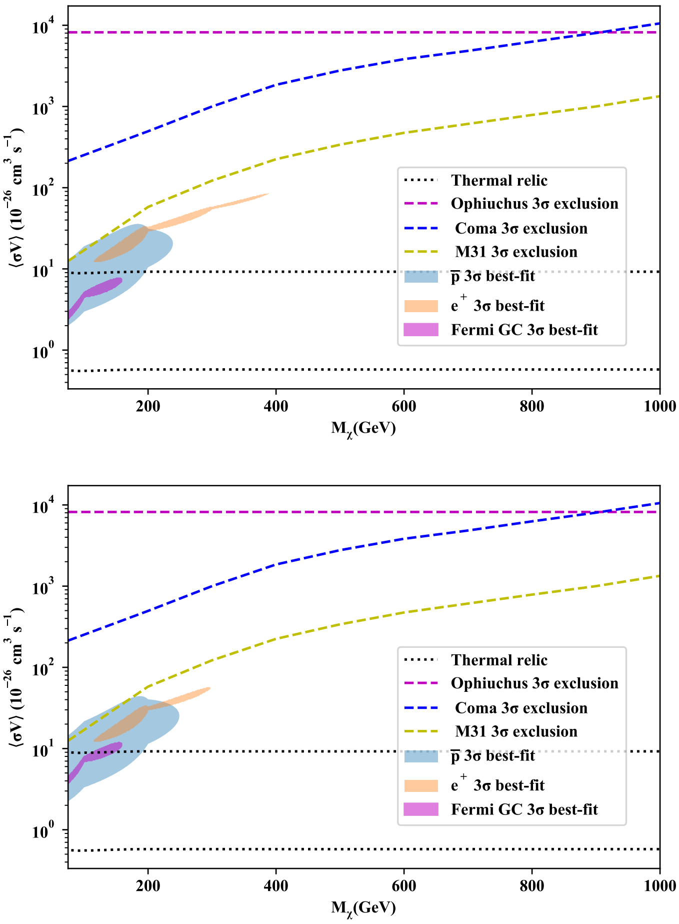

Figure 5.3: The $2 \rightarrow 2$ best-fit parameter space to the AMS-02 positron, anti-proton spectra and Fermi-LAT galactic excesses for NFW halo profile. The contours are 3σ confidence intervals on the M_χ and $\langle \sigma V \rangle$ plane. The thermal relic [187] is denoted as a band to account for uncertainties in the local DM density and halo profile. Dashed lines denote 3σ exclusion limits for M31 (yellow), Coma (blue) and Ophiuchus (Magenta).Top: We have Einasto halo profile case. Bottom: We have NFW halo profile case.

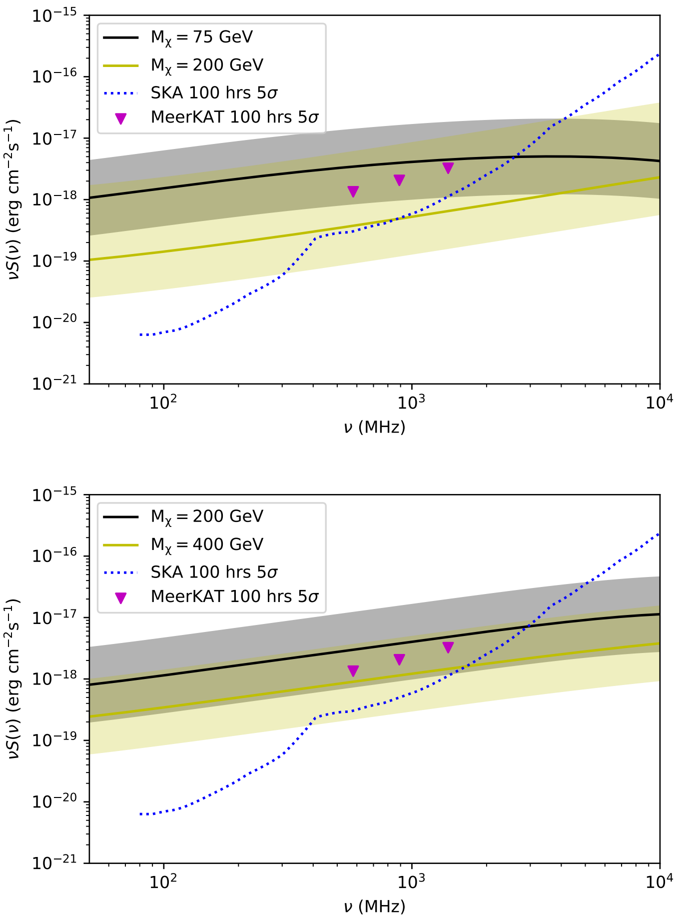

Figure 5.4: Synchrotron radio spectrum prediction for Reticulum II for the Einasto halo profile. The shaded regions accounts for the cross-section uncertainties from the allowed parameter space, as well as those from the J-factor of the halo and magnetic field. Top: We have $2 \to 2$ scattering. Bottom: We have $2 \to 3$ scattering.

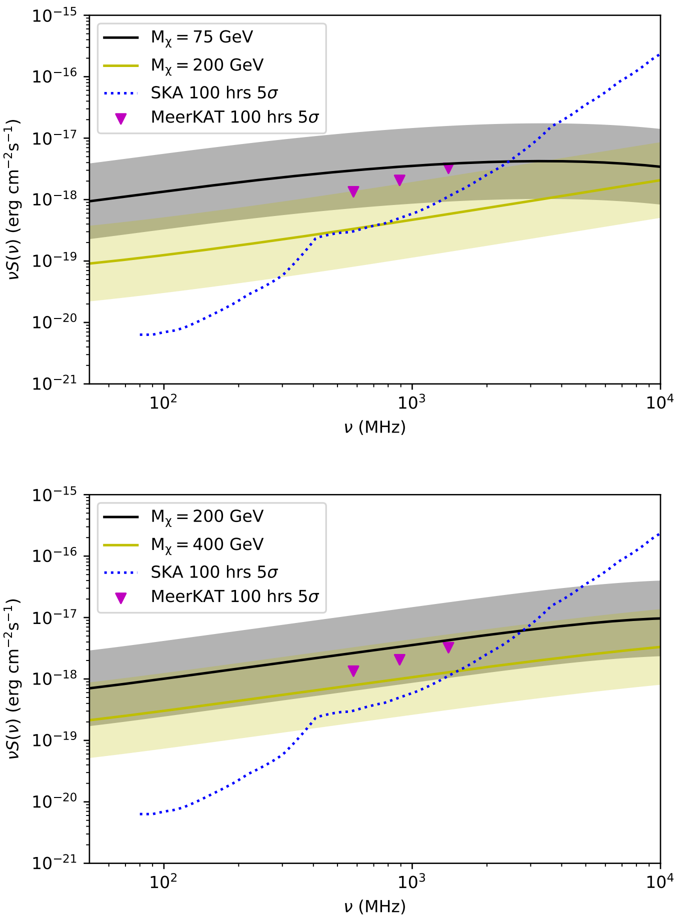

Figure 5.5: Synchrotron radio spectrum prediction for Reticulum II for the Burkert halo profile. The shaded regions accounts for the cross-section uncertainties from the allowed parameter space, as well as those from the J-factor of the halo and magnetic field. Top: We have $2 \to 2$ scattering. Bottom: We have $2 \to 3$ scattering.

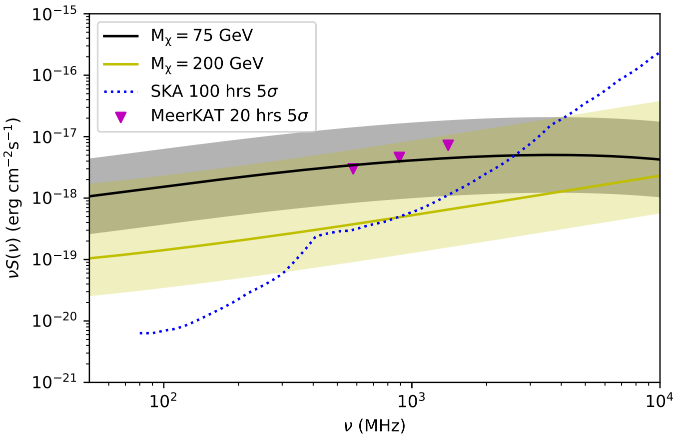

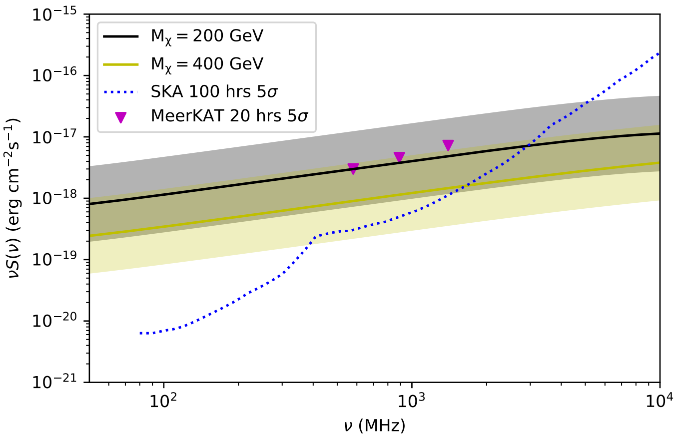

Figure 5.6: Synchrotron radio spectrum prediction for Reticulum II for the Einasto halo profile. The shaded regions accounts for the cross-section uncertainties from the allowed parameter space, as well as those from the J-factor of the halo and magnetic field. Top: We have $2 \rightarrow 2$ scattering. Bottom: We have $2 \rightarrow 3$ scattering.

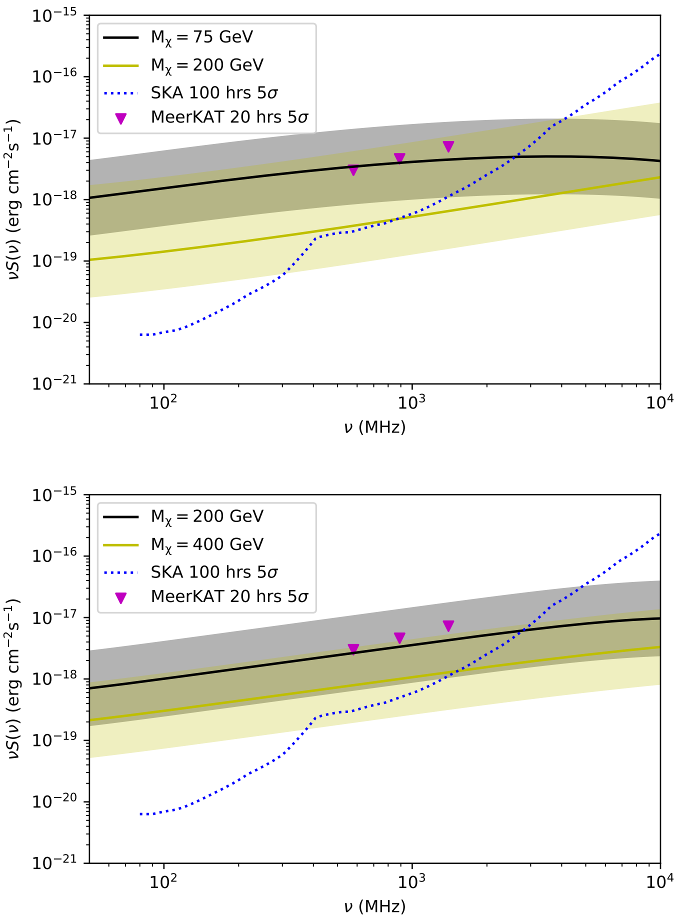

Figure 5.7: Synchrotron radio spectrum prediction for Reticulum II for the Burkert halo profile. The shaded regions accounts for the cross-section uncertainties from the allowed parameter space, as well as those from the J-factor of the halo and magnetic field. Top: We have $2 \rightarrow 2$ scattering. Bottom: We have $2 \rightarrow 3$ scattering.

in both the $2 \to 2$ and $2 \to 3$ cases. Interestingly, $2 \to 3$ induces slightly weaker emissions. Fig. 5.5 shows that Reticulum II with Burkert halo profile yield similar predictions to that of Einasto halo profile. The distinction between the two halo profile predictions is that the Einasto halo profile induces slightly stronger emissions. The estimated sensitivity of the full-SKA [123] can probe the entire uncertainty band at a 5σ confidence interval for 100 hours observations. A somewhat similar but model-independent approach demonstrated the potential of the SKA to probe the radio signal for the Draco dwarf spheroidal galaxy with just 100 hours of observation [217].
In Fig. 5.6 and 5.7, a more realistic observation of 20 hours with MeerKAT was considered. It is remarkable that the lower masses (75 GeV for $2 \to 2$ and 200 GeV for $2 \to 3$) are detectable. This indicates that observation of targets like Reticulum II with MeerKAT will be very beneficial in probing the DM interpretation offered by the Madala hypothesis.

For any prospect 5σ level MeerKAT detection, at least 1600 hours would be necessary. This occurs when $B_0 = 1$ μG and $M_\chi = 200$ GeV. Since detection requires 1600 hours of MeerKAT observation time suggests that it is improbable when $B_0 = 1$ μG. However, by augmenting the sensitivity to 0.5 μJy beam^{-1} can potentially drop the observation time to at least 40 hours. Thus, obtaining sub-micro-Jansky sensitivities allows a more practical possibility of detection (which will notably require the full-SKA [123]). Furthermore, in Ref. [1] MeerKAT sensitivity demonstrates a high constraining power transcending that of the Fermi-LAT data [213].

Chapter 6

Conclusion

In this work, we took a model-dependent route, and the model of interest is the Madala hypothesis. The model was put forward to explain the multi-lepton anomalies seen at the LHC. Furthermore, the Madala hypothesis is used to describe the cosmic ray and gamma ray flux excesses from the Milky Way's galactic centre. The basic recipe is to model how positrons, anti-protons, and gamma rays induced from DM annihilation via S, propagate from the galactic centre to the location of the Earth. The DM annihilation occurs in two distinct scattering processes ($2 \to 2$ and $2 \to 3$). The MED diffusion scenario and three halo profiles, which are the contracted Einasto, Einasto, and NFW halo profile are considered. The modeled fluxes were fit to the AMS-02 and Fermi-LAT data. The best description of the excesses for $2 \to 2$ scattering processes is found at masses below 200 GeV. Additionally, no complete overlap of the constraints to the parameter space derived from the analysis of three excesses is apparent, and of course, we acknowledge that there is unresolved systematics in the data used. It is quite amazing that our assumption of the Madala hypothesis can provide a close clustering of the best-fit regions for the excesses. For $2 \to 3$ we observe a close mutual overlap only for NFW halo for $M_\chi \approx 400 - 450$ GeV. There is no clear overlap of the best-fit regions of the excesses for the "MIN" diffusion scenario. The optimistic diffusion case scenario "MAX" is the only one where it is possible to see the presence of a quite wide overlapping of the best-fit regions derived from the three excesses, even if a value of the cross section higher than the thermal relic one is required.

Subsequently, the parameter spaces of the "MED" diffusion scenario allowed us to assume that $\langle \sigma V \rangle_{22} \approx 10^{-25}$ cm^{3}s^{-1} and $\langle \sigma V \rangle_{23} \approx 2.5 \times 10^{-25}$ cm^{3}s^{-1}, which were used to make synchrotron emission predictions for Coma cluster, Ophiuchus cluster, M31 and Reticulum II. The synchrotron emission predictions for the Coma cluster and Ophiuchus cluster were compared to the available radio data, and the results demonstrate that the Coma cluster radio constraints are superior to those of the Ophiuchus cluster.

Secondly, the induced parameter space that best fits the AMS-02 and Fermi-LAT excesses was compared to 3σ exclusion limits obtained from radio data in M31 as well as Coma and Ophiuchus. M31 shows high constraining power exceeding that of both Coma and Ophiuchus. Significantly, all the exclusion limits do not rule out the Madala hypothesis' ability to explain the observed astrophysical excesses. In Ref. [1] it is confirmed that the model offered by the Madala hypothesis describing both the LHC and astrophysics data simultaneously is not ruled out by the direct DM searches.

The Reticulum II snychrotron emission predictions were compared to the rather conservative MeerKAT sensitivity for the L-band, where visibility taper is elided. The results for the 3 arcminutes observation region is that 5σ detection is possible with just 20 hours of observation for lower masses (75 GeV for $2 \to 2$ scattering and 200 GeV for $2 \to 3$ scattering). In spite of that, in order to survey up to $M_\chi \gtrapprox 200$ GeV, approximately 1600 hours observation might be necessary. Furthermore, the analysis of Reticulum II demonstrates that the Einasto halo profile is more favored than the Burkert halo profile. But the full-SKA can probe the entire uncertainty band for all masses at a 5σ confidence level with just 100 hours observation time. Ref. [1] demonstrated that MeerKAT is characterised by a constraining power transcending that of the Fermi-LAT. This undoubtedly showcases that MeerKAT is at the forefront of DM indirect search.

In near future, as radio instruments enter a new era of high sensitivity while significance at the LHC is increasing, the Madala hypothesis may be able to unpack the elusive nature of DM. Furthermore, with the implementation of the full-SKA in future, predicaments caused by magnetic field structures of dwarf galaxies can potentially be mitigated by rotation measure studies, this will hopefully allow us to produce superior DM limits.
In this work, we did not consider the effects imposed by the boost factor, in particular from Sommerfeld enhancement [218] and sub-clumps in DM halos [35] which can potentially enhance the synchrotron radio emission signal. In literature, substructures (DM sub-clumps) could potentially enhance the radio signal by a factor of $2-3$ depending on the size of the halo[1] for both the NFW and Burkert halo profiles [35]. Therefore, a better constraint on this factor and its inclusion into the calculation presented in this dissertation can significantly yield better DM limits for the Madala hypothesis.

[1]For galaxy clusters like Coma it can be as large as 35.

Bibliography

[1] G. Beck, R. Temo, E. Malwa, M. Kumar, and B. Mellado, "Connecting multi-lepton anomalies at the lhc and in astrophysics with meerkat/ska," *arXiv preprint arXiv:2102.10596*, 2021.

[2] O. Lebedev, H. M. Lee, and Y. Mambrini, "Vector higgs portal dark matter and the invisible higgs," *Physics Letters B*, vol. 707, no. 5, pp. 570–576, 2012.

[3] D. Spolyar, K. Freese, and P. Gondolo, "Dark matter and the first stars: a new phase of stellar evolution," *Physical Review Letters*, vol. 100, no. 5, p. 051101, 2008.

[4] D. N. Spergel, R. Bean, O. Doré, M. Nolta, C. Bennett, J. Dunkley, G. Hinshaw, N. e. Jarosik, E. Komatsu, L. Page, *et al.*, "Three-year wilkinson microwave anisotropy probe (wmap) observations: implications for cosmology," *The Astrophysical Journal Supplement Series*, vol. 170, no. 2, p. 377, 2007.

[5] V. C. Rubin and W. K. Ford Jr, "Rotation of the andromeda nebula from a spectroscopic survey of emission regions," *The Astrophysical Journal*, vol. 159, p. 379, 1970.

[6] F. Zwicky, "The redshift of extragalactic nebulae," *Helv. Phys. Acta*, vol. 6, no. 110, p. 138, 1933.

[7] L. V. Koopmans and T. Treu, "The structure and dynamics of luminous and dark matter in the early-type lens galaxy of 0047–281 at z= 0.485," *The Astrophysical Journal*, vol. 583, no. 2, p. 606, 2003.

[8] L. A. Moustakas and R. B. Metcalf, "Detecting dark matter substructure spectroscopically in strong gravitational lenses," *Monthly Notices of the Royal Astronomical Society*, vol. 339, no. 3, pp. 607–615, 2003.

[9] P. A. Ade, N. Aghanim, M. Arnaud, M. Ashdown, J. Aumont, C. Baccigalupi, A. Banday, R. Barreiro, J. Bartlett, N. Bartolo, *et al.*, "Planck 2015 results-xiii. cosmological parameters," *Astronomy & Astrophysics*, vol. 594, p. A13, 2016.

[10] N. W. Boggess, J. C. Mather, R. Weiss, C. L. Bennett, E. a. Cheng, E. Dwek, S. Gulkis, M. G. Hauser, M. A. Janssen, T. Kelsall, *et al.*, "The cobe mission-its design and performance two years after launch," *The Astrophysical Journal*, vol. 397, pp. 420–429, 1992.

[11] G. Hinshaw, D. Larson, E. Komatsu, D. N. Spergel, C. Bennett, J. Dunkley, M. Nolta, M. Halpern, R. Hill, N. Odegard, *et al.*, "Nine-year wilkinson microwave anisotropy probe (wmap) observations: cosmological parameter results," *The Astrophysical Journal Supplement Series*, vol. 208, no. 2, p. 19, 2013.

[12] K. A. Olive and D. Thomas, "A big band nucleosynthesis likelihood analysis of the baryon-to-photon ratio and the number of light particle degrees of freedom," *Astroparticle Physics*, vol. 7, no. 1-2, pp. 27–34, 1997.

[13] S. Sarkar, "Big bang nucleosynthesis and physics beyond the standard model," *Reports on Progress in Physics*, vol. 59, no. 12, p. 1493, 1996.

[14] A. Collaboration, G. Aad, *et al.*, "The atlas experiment at the cern large hadron collider. jinst, 3 (s08003), 2008," *Chatrchyan et al., The CMS experiment at the CERN LHC JINST*, vol. 3, p. S08004, 2008.

[15] S. von Buddenbrock, N. Chakrabarty, A. S. Cornell, D. Kar, M. Kumar, T. Mandal, B. Mellado, B. Mukhopadhyaya, R. G. Reed, and X. Ruan, "Phenomenological signatures of additional scalar bosons at the LHC," *Eur. Phys. J. C*, vol. 76, no. 10, p. 580, 2016.

[16] S. von Buddenbrock, N. Chakrabarty, A. S. Cornell, D. Kar, M. Kumar, T. Mandal, B. Mellado, B. Mukhopadhyaya, and R. G. Reed, "The compatibility of lhc run 1 data with a heavy scalar of mass around 270\, gev," *arXiv preprint arXiv:1506.00612*, 2015.

[17] S. von Buddenbrock, A. S. Cornell, A. F. Mohammed, M. Kumar, B. Mellado, and X. Ruan, "Multi-lepton signatures of additional scalar bosons beyond the standard model at the lhc," *Journal of Physics G: Nuclear and Particle Physics*, vol. 45, no. 11, p. 115003, 2018.

[18] S. von Buddenbrock, "Exploring lhc run 1 and 2 data using the madala hypothesis," in *Journal of Physics: Conference Series*, vol. 878, p. 012030, IOP Publishing, 2017.

[19] G. Beck and S. Colafrancesco, "Exploring the potential of the dark matter candidate from the madala hypothesis with multi-frequency indirect detection," *arXiv preprint arXiv:1707.07940*, 2017.

[20] G. Beck and S. Colafrancesco, "What can gamma-rays from space tell us about the madala hypothesis?," in *Journal of Physics: Conference Series*, vol. 889, p. 012006, IOP Publishing, 2017.

[21] G. Beck and S. Colafrancesco, "Gamma-rays and lhc-inspired dark matter," *arXiv preprint arXiv:1812.00691*, 2018.

[22] M. Aguilar, L. A. Cavasonza, G. Ambrosi, L. Arruda, N. Attig, P. Azzarello, A. Bachlechner, F. Barao, A. Barrau, L. Barrin, *et al.*, "Towards understanding the origin of cosmic-ray positrons," *Physical review letters*, vol. 122, no. 4, p. 041102, 2019.

[23] M. Aguilar, L. A. Cavasonza, B. Alpat, G. Ambrosi, L. Arruda, N. Attig, S. Aupetit, P. Azzarello, A. Bachlechner, F. Barao, *et al.*, "Antiproton flux, antiproton-to-proton flux ratio, and properties of elementary particle fluxes in primary cosmic rays measured with the alpha magnetic spectrometer on the international space station," *Physical Review Letters*, vol. 117, no. 9, p. 091103, 2016.

[24] M. Ackermann, M. Ajello, A. Albert, W. Atwood, L. Baldini, J. Ballet, G. Barbiellini, D. Bastieri, R. Bellazzini, E. Bissaldi, *et al.*, "The fermi galactic center gev excess and implications for dark matter," *The Astrophysical Journal*, vol. 840, no. 1, p. 43, 2017.

[25] E. Pécontal, T. Buchert, P. Di Stefano, Y. Copin, and K. Freese, "Review of observational evidence for dark matter in the universe and in upcoming searches for dark stars," *European Astronomical Society Publications Series*, vol. 36, pp. 113–126, 2009.

[26] Y. Sofue, "The most completely sampled rotation curves for galaxies," *arXiv preprint astro-ph/9507098*, 1995.

[27] D. M. Wittman, J. A. Tyson, D. Kirkman, I. Dell'Antonio, and G. Bernstein, "Detection of weak gravitational lensing distortions of distant galaxies by cosmic dark matter at large scales," *Nature*, vol. 405, no. 6783, pp. 143–148, 2000.

[28] D. Clowe, M. Bradač, A. H. Gonzalez, M. Markevitch, S. W. Randall, C. Jones, and D. Zaritsky, "A direct empirical proof of the existence of dark matter," *The Astrophysical Journal Letters*, vol. 648, no. 2, p. L109, 2006.

[29] C. Sheng, H. Liu, Y. Wang, S. Zhu, and D. Genov, "Trapping light by mimicking gravitational lensing," *Nature Photonics*, vol. 7, no. 11, pp. 902–906, 2013.

[30] M. Bartelmann and P. Schneider, "Weak gravitational lensing," *Physics Reports*, vol. 340, no. 4-5, pp. 291–472, 2001.

[31] J. K. A.-M. et al., "The fourth data release of the sloan digital sky survey," 2005.

[32] R. Massey, T. Kitching, and J. Richard, "The dark matter of gravitational lensing," *Reports on Progress in Physics*, vol. 73, no. 8, p. 086901, 2010.

[33] E. Komatsu, K. M. Smith, J. Dunkley, C. L. Bennett, B. Gold, G. Hinshaw, N. Jarosik, D. Larson, M. R. Nolta, L. Page, D. N. Spergel, M. Halpern, R. S. Hill, A. Kogut, M. Limon, S. S. Meyer, N. Odegard, G. S. Tucker, J. L. Weiland, E. Wollack, and E. L. Wright, "Seven-year wilkinson microwave anisotropy probe (wmap) observations: Cosmological interpretation," 2010.

[34] C. Bennett, A. Banday, K. Gorski, G. Hinshaw, P. Jackson, P. Keegstra, A. Kogut, G. F. Smoot, D. Wilkinson, and E. Wright, "Four-year cobe* dmr cosmic microwave background observations: maps and basic results," *The Astrophysical Journal Letters*, vol. 464, no. 1, p. L1, 1996.

[35] G. M. Beck, *Multi-messenger probes of dark matter, from radio to multi-frequency.* PhD thesis, 2016.

[36] T. P. Walker, G. Steigman, D. N. Schramm, K. A. Olive, and H.-S. Kang, "Primordial nucleosynthesis redux," *The Big Bang And Other Explosions In Nuclear And Particle Astrophysics*, pp. 43–61, 1991.

[37] P. J. E. Peebles, D. Schramm, E. L. Turner, and R. Kron, "The case for the relativistic hot big bang cosmology," *Nature*, vol. 352, no. 6338, pp. 769–776, 1991.

[38] K. A. Olive, D. N. Schramm, G. Steigman, and T. P. Walker, "Big-bang nucleosynthesis revisited," *Physics Letters B*, vol. 236, no. 4, pp. 454–460, 1990.

[39] D. Baumann, "Cosmology: Part iii mathematical tripos," *University lecture notes*, vol. 56, 2014.

[40] G. Jungman, M. Kamionkowski, and K. Griest, "Supersymmetric dark matter," *Physics Reports*, vol. 267, no. 5-6, pp. 195–373, 1996.

[41] S. D. White, C. S. Frenk, and M. Davis, "Clustering in a neutrino-dominated universe," *The Astrophysical Journal*, vol. 274, pp. L1–L5, 1983.

[42] G. Bertone, "The moment of truth for wimp dark matter," *Nature*, vol. 468, no. 7322, pp. 389–393, 2010.

[43] R. J. Scherrer and M. S. Turner, "On the relic, cosmic abundance of stable, weakly interacting massive particles," *Physical Review D*, vol. 33, no. 6, p. 1585, 1986.

[44] B. W. Lee and S. Weinberg, "Cosmological lower bound on heavy-neutrino masses," *Physical Review Letters*, vol. 39, no. 4, p. 165, 1977.

[45] J. Edsjö and P. Gondolo, "Neutralino relic density including coannihilations," *Physical Review D*, vol. 56, no. 4, p. 1879, 1997.

[46] M. Cannoni, "Exact theory of freeze-out," *The European Physical Journal C*, vol. 75, no. 3, pp. 1–10, 2015.

[47] Y. Lu, H. Mo, N. Katz, and M. D. Weinberg, "On the origin of cold dark matter halo density profiles," *Monthly Notices of the Royal Astronomical Society*, vol. 368, no. 4, pp. 1931–1940, 2006.

[48] R. R. Mekuria, *Multi-wavelength emissions from dark matter annihilation processes in galaxy clusters using cosmological simulations*. PhD thesis.

[49] J. F. Navarro, C. S. Frenk, and S. D. White, "A universal density profile from hierarchical clustering," *The Astrophysical Journal*, vol. 490, no. 2, p. 493, 1997.

[50] J. F. Navarro, C. S. Frenk, and S. D. M. White, "The Structure of cold dark matter halos," *Astrophys. J.*, vol. 462, pp. 563–575, 1996.

[51] D. Merritt, A. W. Graham, B. Moore, J. Diemand, and B. Terzić, "Empirical models for dark matter halos. i. nonparametric construction of density profiles and comparison with parametric models," *The Astronomical Journal*, vol. 132, no. 6, p. 2685, 2006.

[52] J. F. Navarro, A. Ludlow, V. Springel, J. Wang, M. Vogelsberger, S. D. White, A. Jenkins, C. S. Frenk, and A. Helmi, "The diversity and similarity of simulated cold dark matter haloes," *Monthly Notices of the Royal Astronomical Society*, vol. 402, no. 1, pp. 21–34, 2010.

[53] J. Einasto, "On galactic descriptive functions," *Astronomische Nachrichten*, vol. 291, p. 97, 1969.

[54] P. B. Tissera, S. D. White, S. Pedrosa, and C. Scannapieco, "Dark matter response to galaxy formation," *Monthly Notices of the Royal Astronomical Society*, vol. 406, no. 2, pp. 922–935, 2010.

[55] A. Burkert, "The structure of dark matter halos in dwarf galaxies," *The Astrophysical Journal Letters*, vol. 447, no. 1, p. L25, 1995.

[56] R. A. Flores and J. R. Primack, "Observational and theoretical constraints on singular dark matter halos," *arXiv preprint astro-ph/9402004*, 1994.

[57] W. De Blok, F. Walter, E. Brinks, C. Trachternach, S. Oh, and R. Kennicutt Jr, "High-resolution rotation curves and galaxy mass models from things," *The Astronomical Journal*, vol. 136, no. 6, p. 2648, 2008.

[58] A. Loeb and M. Zaldarriaga, "Small-scale power spectrum of cold dark matter," *Physical Review D*, vol. 71, no. 10, p. 103520, 2005.

[59] S. Ghigna, B. Moore, F. Governato, G. Lake, T. Quinn, and J. Stadel, "Dark matter haloes within clusters," *Monthly Notices of the Royal Astronomical Society*, vol. 300, no. 1, pp. 146–162, 1998.

[60] J. Diemand and B. Moore, "The structure and evolution of cold dark matter halos," *Advanced Science Letters*, vol. 4, no. 2, pp. 297–310, 2011.

[61] E. A. Baltz, J. E. Taylor, and L. L. Wai, "Can astrophysical gamma-ray sources mimic dark matter annihilation in galactic satellites?," *The Astrophysical Journal Letters*, vol. 659, no. 2, p. L125, 2007.

[62] L. Bergström, J. Edsjö, P. Gondolo, and P. Ullio, "Clumpy neutralino dark matter," *Physical Review D*, vol. 59, no. 4, p. 043506, 1999.

[63] L. G. van den Aarssen, T. Bringmann, and Y. C. Goedecke, "Thermal decoupling and the smallest subhalo mass in dark matter models with sommerfeld-enhanced annihilation rates," *Physical Review D*, vol. 85, no. 12, p. 123512, 2012.

[64] K. Bechtol, A. Drlica-Wagner, E. Balbinot, A. Pieres, J. D. Simon, B. Yanny, B. Santiago, R. H. Wechsler, J. Frieman, A. Walker, *et al.*, "Eight new milky way companions discovered in first-year dark energy survey data," *The Astrophysical Journal*, vol. 807, no. 1, p. 50, 2015.

[65] A. Drlica-Wagner, K. Bechtol, E. Rykoff, E. Luque, A. Queiroz, Y.-Y. Mao, R. H. Wechsler, J. D. Simon, B. Santiago, B. Yanny, *et al.*, "Eight ultra-faint galaxy candidates discovered in year two of the dark energy survey," *The Astrophysical Journal*, vol. 813, no. 2, p. 109, 2015.

[66] S. Y. Kim, A. H. Peter, and J. R. Hargis, "There is no missing satellites problem," *arXiv preprint arXiv:1711.06267*, 2017.

[67] M. Boylan-Kolchin, J. S. Bullock, and M. Kaplinghat, "The milky way's bright satellites as an apparent failure of λcdm," *Monthly Notices of the Royal Astronomical Society*, vol. 422, no. 2, pp. 1203–1218, 2012.

[68] J. Diemand, M. Kuhlen, P. Madau, M. Zemp, B. Moore, D. Potter, and J. Stadel, "Clumps and streams in the local dark matter distribution," *Nature*, vol. 454, no. 7205, pp. 735–738, 2008.

[69] V. Springel, J. Wang, M. Vogelsberger, A. Ludlow, A. Jenkins, A. Helmi, J. F. Navarro, C. S. Frenk, and S. D. White, "The aquarius project: the subhaloes of galactic haloes," *Monthly Notices of the Royal Astronomical Society*, vol. 391, no. 4, pp. 1685–1711, 2008.

[70] J. Diemand, M. Kuhlen, and P. Madau, "Formation and evolution of galaxy dark matter halos and their substructure," *The Astrophysical Journal*, vol. 667, no. 2, p. 859, 2007.

[71] E. N. Kirby, J. S. Bullock, M. Boylan-Kolchin, M. Kaplinghat, and J. G. Cohen, "The dynamics of isolated local group galaxies," *Monthly Notices of the Royal Astronomical Society*, vol. 439, no. 1, pp. 1015–1027, 2014.

[72] E. J. Tollerud, M. Boylan-Kolchin, and J. S. Bullock, "M31 satellite masses compared to λcdm subhaloes," *Monthly Notices of the Royal Astronomical Society*, vol. 440, no. 4, pp. 3511–3519, 2014.

[73] E. Papastergis and F. Shankar, "An assessment of the "too big to fail" problem for field dwarf galaxies in view of baryonic feedback effects," *Astronomy & Astrophysics*, vol. 591, p. A58, 2016.

[74] T. M. Undagoitia and L. Rauch, "Dark matter direct-detection experiments," *Journal of Physics G: Nuclear and Particle Physics*, vol. 43, no. 1, p. 013001, 2015.

[75] M. W. Goodman and E. Witten, "Detectability of certain dark-matter candidates," *Physical Review D*, vol. 31, no. 12, p. 3059, 1985.

[76] J. Lewin and P. Smith, "Review of mathematics, numerical factors, and corrections for dark matter experiments based on elastic nuclear recoil," *Astroparticle Physics*, vol. 6, no. 1, pp. 87–112, 1996.

[77] D. G. Cerdeno and A. M. Green, "Direct detection of wimps," *arXiv preprint arXiv:1002.1912*, 2010.

[78] A. K. Drukier, K. Freese, and D. N. Spergel, "Detecting cold dark-matter candidates," *Physical Review D*, vol. 33, no. 12, p. 3495, 1986.

[79] C. J. Copi, J. Heo, and L. M. Krauss, "Directional sensitivity, wimp detection, and the galactic halo," *Physics Letters B*, vol. 461, no. 1-2, pp. 43–48, 1999.

[80] D. N. Spergel, "Motion of the earth and the detection of weakly interacting massive particles," *Physical Review D*, vol. 37, no. 6, p. 1353, 1988.

[81] D. P. Snowden-Ifft, C. J. Martoff, and J. M. Burwell, "Low pressure negative ion time projection chamber for dark matter search," *Physical Review D*, vol. 61, no. 10, p. 101301, 2000.

[82] M. Felizardo, T. Girard, T. Morlat, A. Fernandes, A. Ramos, J. Marques, A. Kling, J. Puibasset, M. Auguste, D. Boyer, *et al.*, "The simple phase ii dark matter search," *Physical Review D*, vol. 89, no. 7, p. 072013, 2014.

[83] S. Archambault, E. Behnke, P. Bhattacharjee, S. Bhattacharya, X. Dai, M. Das, A. Davour, F. Debris, N. Dhungana, J. Farine, *et al.*, "Constraints on low-mass wimp interactions on 19f from picasso," *Physics Letters B*, vol. 711, no. 2, pp. 153–161, 2012.

[84] E. Behnke, J. Behnke, S. Brice, D. Broemmelsiek, J. Collar, A. Conner, P. Cooper, M. Crisler, C. Dahl, D. Fustin, *et al.*, "First dark matter search results from a 4-kg cf 3 i bubble chamber operated in a deep underground site," *Physical Review D*, vol. 86, no. 5, p. 052001, 2012.

[85] E. Aprile, J. Aalbers, F. Agostini, M. Alfonsi, F. Amaro, M. Anthony, F. Arneodo, P. Barrow, L. Baudis, B. Bauermeister, *et al.*, "Xenon100 dark matter results from a combination of 477 live days," *Physical Review D*, vol. 94, no. 12, p. 122001, 2016.

[86] E. Aprile, J. Aalbers, F. Agostini, M. Alfonsi, F. Amaro, M. Anthony, F. Arneodo, P. Barrow, L. Baudis, B. Bauermeister, *et al.*, "First dark matter search results from the xenon1t experiment," *Physical review letters*, vol. 119, no. 18, p. 181301, 2017.

[87] D. Akerib, S. Alsum, H. Araújo, X. Bai, A. Bailey, J. Balajthy, P. Beltrame, E. Bernard, A. Bernstein, T. Biesiadzinski, *et al.*, "Results from a search for dark matter in the complete lux exposure," *Physical review letters*, vol. 118, no. 2, p. 021303, 2017.

[88] X. Cui, A. Abdukerim, W. Chen, X. Chen, Y. Chen, B. Dong, D. Fang, C. Fu, K. Giboni, F. Giuliani, *et al.*, "Dark matter results from 54-ton-day exposure of pandax-ii experiment," *Physical review letters*, vol. 119, no. 18, p. 181302, 2017.

[89] M. Schumann, "Dark matter search with liquid noble gases," *arXiv preprint arXiv:1206.2169*, 2012.

[90] E. Armengaud, Q. Arnaud, C. Augier, A. Benoît, L. Bergé, T. Bergmann, J. Billard, T. De Boissière, G. Bres, A. Broniatowski, *et al.*, "Performance of the edelweiss-iii experiment for direct dark matter searches," *Journal of Instrumentation*, vol. 12, no. 08, p. P08010, 2017.

[91] C. E. Aalseth, P. S. Barbeau, J. Colaresi, J. Collar, J. D. Leon, J. E. Fast, N. Fields, T. W. Hossbach, A. Knecht, M. S. Kos, *et al.*, "Cogent: A search for low-mass dark matter using p-type point contact germanium detectors," *Physical Review D*, vol. 88, no. 1, p. 012002, 2013.

[92] F. Petricca, G. Angloher, P. Bauer, A. Bento, C. Bucci, L. Canonica, X. Defay, A. Erb, F. v Feilitzsch, N. F. Iachellini, *et al.*, "First results on low-mass dark matter from the cresst-iii experiment," in *Journal*

of Physics: Conference Series, vol. 1342, p. 012076, IOP Publishing, 2020.

[93] R. Bernabei, P. Belli, F. Cappella, R. Cerulli, C. Dai, A. d'Angelo, H. He, A. Incicchitti, H. Kuang, X. Ma, *et al.*, "New results from dama/libra," *The European Physical Journal C*, vol. 67, no. 1, pp. 39–49, 2010.

[94] J. Cooley, "Overview of non-liquid noble direct detection dark matter experiments," *arXiv preprint arXiv:1410.4960*, 2014.

[95] O. S. Brüning, P. Collier, P. Lebrun, S. Myers, R. Ostojic, J. Poole, and P. Proudlock, "Lhc design report. cern, geneva, 2004," *URL http://cdsweb. cern. ch/record/782076*.

[96] K. Kong, "Measuring properties of dark matter at the lhc," in *AIP Conference Proceedings*, vol. 1604, pp. 381–388, American Institute of Physics, 2014.

[97] T. Behnke, "The international linear collider," *Fortschritte der Physik*, vol. 58, no. 7-9, pp. 622–627, 2010.

[98] G. Aad, E. Abat, J. Abdallah, A. Abdelalim, A. Abdesselam, B. Abi, M. Abolins, H. Abramowicz, E. Acerbi, B. Acharya, *et al.*, "The atlas experiment at the cern large hadron collider," *Journal of instrumentation*, vol. 3, p. S08003, 2008.

[99] C. Collaboration, S. Chatrchyan, G. Hmayakyan, V. Khachatryan, A. Sirunyan, W. Adam, T. Bauer, T. Bergauer, H. Bergauer, M. Dragicevic, *et al.*, "The cms experiment at the cern lhc," *JInst*, vol. 3, p. S08004, 2008.

[100] S. Chatrchyan, V. Khachatryan, A. M. Sirunyan, A. Tumasyan, W. Adam, E. Aguilo, T. Bergauer, M. Dragicevic, J. Erö, C. Fabjan, *et al.*, "Search for dark matter and large extra dimensions in monojet events in pp collisions at $\sqrt{s}$ =7 tev," *Journal of High Energy Physics*, vol. 2012, no. 9, pp. 1–37, 2012.

[101] G. Aad, T. Abajyan, B. Abbott, J. Abdallah, S. A. Khalek, A. Abdelalim, R. Aben, B. Abi, M. Abolins, O. Abouzeid, *et al.*, "Search for dark matter candidates and large extra dimensions in events with a jet and missing transverse momentum with the atlas detector," *Journal of High Energy Physics*, vol. 2013, no. 4, pp. 1–51, 2013.

[102] W. Atwood, A. A. Abdo, M. Ackermann, W. Althouse, B. Anderson, M. Axelsson, L. Baldini, J. Ballet, D. Band, G. Barbiellini, *et al.*, "The large area telescope on the fermi gamma-ray space telescope mission," *The Astrophysical Journal*, vol. 697, no. 2, p. 1071, 2009.

[103] H. Abdallah, A. Abramowski, F. Aharonian, F. A. Benkhali, A. Akhperjanian, E. Angüner, M. Arrieta, P. Aubert, M. Backes, A. Balzer, *et al.*, "Search for dark matter annihilations towards the inner galactic halo from 10 years of observations with hess," *Physical Review Letters*, vol. 117, no. 11, p. 111301, 2016.

[104] J. Holder, E. Aliu, T. Arlen, T. Aune, M. Beilicke, W. Benbow, M. Böttcher, A. Bouvier, J. Buckley, V. Bugaev, *et al.*, "Veritas: Status and highlights," *arXiv preprint arXiv:1111.1225*, 2011.

[105] J. Aleksić, S. Ansoldi, L. A. Antonelli, P. Antoranz, A. Babic, P. Bangale, U. B. De Almeida, J. Barrio, J. B. González, W. Bednarek, *et al.*, "Optimized dark matter searches in deep observations of segue 1 with magic," *Journal of Cosmology and Astroparticle Physics*, vol. 2014, no. 02, p. 008, 2014.

[106] M. Actis, G. Agnetta, F. Aharonian, A. Akhperjanian, J. Aleksić, E. Aliu, D. Allan, I. Allekotte, F. Antico, L. Antonelli, *et al.*, "Design concepts for the cherenkov telescope array cta: an advanced facility for ground-based high-energy gamma-ray astronomy," *Experimental Astronomy*, vol. 32, no. 3, pp. 193–316, 2011.

[107] L. Bergström, T. Bringmann, and J. Edsjö, "Complementarity of direct dark matter detection and indirect detection through gamma rays," *Phys. Rev. D*, vol. 83, p. 045024, Feb 2011.

[108] M. Cirelli, "Status of indirect (and direct) dark matter searches," *arXiv preprint arXiv:1511.02031*, 2015.

[109] I. V. Moskalenko, G. Jóhannesson, E. Orlando, T. Porter, A. Strong, and A. Vladimirovd, "Galprop code for galactic cosmic ray propagation and associated photon emissions," *These Proceedings (July, 2017)*, 2015.

[110] D. Gaggero, "Connections between cosmic-ray physics, gamma-ray data analysis and dark matter detection," *arXiv preprint arXiv:1509.09050*, 2015.

[111] S. Barwick, J. Beatty, A. Bhattacharyya, C. Bower, C. Chaput, S. Coutu, G. De Nolfo, J. Knapp, D. Lowder, S. McKee, *et al.*, "Measurements of the cosmic-ray positron fraction from 1 to 50 gev," *The Astrophysical Journal Letters*, vol. 482, no. 2, p. L191, 1997.

[112] C. Grimani, S. Stephens, F. Cafagna, G. Basini, R. Bellotti, M. Brunetti, M. Circella, A. Codino, C. De Marzo, M. De Pascale, *et al.*, "Measurements of the absolute energy spectra of cosmic-ray positrons and electrons above 7 gev," *Astronomy & Astrophysics*, vol. 392, no. 1, pp. 287–294, 2002.

[113] O. Adriani, G. Barbarino, G. Bazilevskaya, R. Bellotti, A. Bianco, M. Boezio, E. Bogomolov, M. Bongi, V. Bonvicini, S. Bottai, *et al.*, "Cosmic-ray positron energy spectrum measured by pamela," *Physical review letters*, vol. 111, no. 8, p. 081102, 2013.

[114] G. Ambrosi, Q. An, R. Asfandiyarov, P. Azzarello, P. Bernardini, B. Bertucci, M. Cai, J. Chang, D. Chen, H. Chen, *et al.*, "Direct detection of a break in the teraelectronvolt cosmic-ray spectrum of electrons and positrons," *Nature*, vol. 552, no. 7683, p. 63, 2017.

[115] P.-F. Yin, Z.-H. Yu, Q. Yuan, and X.-J. Bi, "Pulsar interpretation for the ams-02 result," *Physical Review D*, vol. 88, no. 2, p. 023001, 2013.

[116] J. Feng and H.-H. Zhang, "Pulsar interpretation of lepton spectra measured by ams-02," *The European Physical Journal C*, vol. 76, no. 5, pp. 1–13, 2016.

[117] E. Borriello, A. Cuoco, and G. Miele, "Radio constraints on dark matter annihilation in the galactic halo and its substructures," *Physical Review D*, vol. 79, no. 2, p. 023518, 2009.

[118] S. Colafrancesco, S. Profumo, and P. Ullio, "Detecting dark matter wimps in the draco dwarf: A multiwavelength perspective," *Physical Review D*, vol. 75, no. 2, p. 023513, 2007.

[119] S. Colafrancesco and B. Melé, "Neutralinos and the origin of radio halos in clusters of galaxies," *The Astrophysical Journal*, vol. 562, no. 1, p. 24, 2001.

[120] M. Regis, S. Colafrancesco, S. Profumo, W. De Blok, M. Massardi, and L. Richter, "Local group dsph radio survey with atca (iii): constraints on particle dark matter," *Journal of Cosmology and Astroparticle Physics*, vol. 2014, no. 10, p. 016, 2014.

[121] M. Regis, L. Richter, and S. Colafrancesco, “Dark matter in the reticulum ii dsph: a radio search,” *Journal of Cosmology and Astroparticle Physics*, vol. 2017, no. 07, p. 025, 2017.

[122] J. M. Marr, R. L. Snell, and S. E. Kurtz, *Fundamentals of radio astronomy: observational methods*, vol. 13. CRC Press, 2015.

[123] R. Braun, A. Bonaldi, T. Bourke, E. Keane, and J. Wagg, “Anticipated performance of the square kilometre array–phase 1 (ska1),” *arXiv preprint arXiv:1912.12699*, 2019.

[124] M. K. Gaillard, P. D. Grannis, and F. J. Sciulli, “The standard model of particle physics,” *Reviews of Modern Physics*, vol. 71, no. 2, p. S96, 1999.

[125] https://commons.wikimedia.org/wiki/File:Standard_Model_of_Elementary_Particles_dark.svg. Accessed: 2021-09-30.

[126] S. Chatrchyan, V. Khachatryan, A. M. Sirunyan, A. Tumasyan, W. Adam, E. Aguilo, T. Bergauer, M. Dragicevic, J. Erö, C. Fabjan, *et al.*, “Observation of a new boson at a mass of 125 gev with the cms experiment at the lhc,” *Physics Letters B*, vol. 716, no. 1, pp. 30–61, 2012.

[127] A. Collaboration *et al.*, “Observation of a new particle in the search for the standard model higgs boson with the atlas detector at the lhc,” 2012.

[128] C. Giganti, S. Lavignac, and M. Zito, “Neutrino oscillations: the rise of the pmns paradigm,” *Progress in Particle and Nuclear Physics*, vol. 98, pp. 1–54, 2018.

[129] L. Canetti, M. Drewes, and M. Shaposhnikov, “Matter and antimatter in the universe,” *New Journal of Physics*, vol. 14, no. 9, p. 095012, 2012.

[130] S. von Buddenbrock, A. S. Cornell, M. Kumar, and B. Mellado, “The madala hypothesis with run 1 and 2 data at the lhc,” in *Journal of Physics: Conference Series*, vol. 889, p. 012020, IOP Publishing, 2017.

[131] S. von Buddenbrock, N. Chakrabarty, A. S. Cornell, D. Kar, M. Kumar, T. Mandal, B. Mellado, B. Mukhopadhyaya, R. G. Reed, and X. Ruan, “Phenomenological signatures of additional scalar bosons at the lhc,” *The European Physical Journal C*, vol. 76, no. 10, p. 580, 2016.

[132] M. Kumar, S. von Buddenbrook, N. Chakrabarty, A. S. Cornell, D. Kar, T. Mandal, B. Mellado, B. Mukhopadhyaya, and R. G. Reed, "The impact of additional scalar bosons at the lhc," in *Journal of Physics: Conference Series*, vol. 802, p. 012007, IOP Publishing, 2017.

[133] S. von Buddenbrock, A. S. Cornell, Y. Fang, A. F. Mohammed, M. Kumar, B. Mellado, and K. G. Tomiwa, "The emergence of multi-lepton anomalies at the lhc and their compatibility with new physics at the ew scale," *Journal of High Energy Physics*, vol. 2019, no. 10, pp. 1–41, 2019.

[134] O. Fischer, B. Mellado, S. Antusch, E. Bagnaschi, S. Banerjee, G. Beck, B. Belfatto, M. Bellis, Z. Berezhiani, M. Blanke, *et al.*, "Unveiling hidden physics at the lhc," *arXiv preprint arXiv:2109.06065*, 2021.

[135] A. Crivellin, Y. Fang, O. Fischer, A. Kumar, M. Kumar, E. Malwa, B. Mellado, N. Rapheeha, X. Ruan, and Q. Sha, "Accumulating evidence for the associate production of a neutral scalar with mass around 151 gev," *arXiv preprint arXiv:2109.02650*, 2021.

[136] G. Aad, B. Abbott, J. Abdallah, S. Abdel Khalek, R. Aben, B. Abi, J. M. Izen, M. Leyton, X. Lou, H. Namasivayam, *et al.*, "Measurements of fiducial and differential cross sections for higgs boson production in the diphoton decay channel at s= 8 tev with atlas," 2014.

[137] G. Aad, B. Abbott, J. Abdallah, S. A. Khalek, R. Aben, B. Abi, M. Abolins, O. AbouZeid, H. Abramowicz, H. Abreu, *et al.*, "Fiducial and differential cross sections of higgs boson production measured in the four-lepton decay channel in pp collisions at s= 8tev with the atlas detector," *Physics Letters B*, vol. 738, pp. 234–253, 2014.

[138] S. Von Buddenbrock, A. S. Cornell, E. D. Iarilala, M. Kumar, B. Mellado, X. Ruan, and E. M. Shrif, "Constraints on a 2hdm with a singlet scalar and implications in the search for heavy bosons at the lhc," *Journal of Physics G: Nuclear and Particle Physics*, vol. 46, no. 11, p. 115001, 2019.

[139] J. Alwall, M. Herquet, F. Maltoni, O. Mattelaer, and T. Stelzer, "Madgraph 5: going beyond," *Journal of High Energy Physics*, vol. 2011, no. 6, pp. 1–40, 2011.

[140] T. Sjöstrand, S. Mrenna, and P. Skands, "A brief introduction to pythia 8.1," *Computer Physics Communications*, vol. 178, no. 11, pp. 852–867, 2008.

[141] M. Cirelli, G. Corcella, A. Hektor, G. Hütsi, M. Kadastik, P. Panci, M. Raidal, F. Sala, and A. Strumia, "Pppc 4 dm id: a poor particle physicist cookbook for dark matter indirect detection," *Journal of Cosmology and Astroparticle Physics*, vol. 2011, no. 03, p. 051, 2011.

[142] P. Salati, "Indirect and direct dark matter detection ," *PoS*, vol. cargese, p. 009, 2009.

[143] E. Nardi, F. Sannino, and A. Strumia, "Decaying dark matter can explain the e±excesses," *Journal of Cosmology and Astroparticle Physics*, vol. 2009, no. 01, p. 043, 2009.

[144] M. Cirelli, R. Franceschini, and A. Strumia, "Minimal dark matter predictions for galactic positrons, anti-protons, photons," *Nuclear physics B*, vol. 800, no. 1-2, pp. 204–220, 2008.

[145] E. A. Baltz and J. Edsjö, "Positron propagation and fluxes from neutralino annihilation in the halo," *Physical Review D*, vol. 59, no. 2, p. 023511, 1998.

[146] J. Hisano, S. Matsumoto, O. Saito, and M. Senami, "Heavy wino-like neutralino dark matter annihilation into antiparticles," *Physical Review D*, vol. 73, no. 5, p. 055004, 2006.

[147] D. Maurin, F. Donato, R. Taillet, and P. Salati, "Cosmic rays below z= 30 in a diffusion model: new constraints on propagation parameters," *The Astrophysical Journal*, vol. 555, no. 2, p. 585, 2001.

[148] J. Buch, M. Cirelli, G. Giesen, and M. Taoso, "Pppc 4 dm secondary: a poor particle physicist cookbook for secondary radiation from dark matter," *Journal of Cosmology and Astroparticle Physics*, vol. 2015, no. 09, p. 037, 2015.

[149] L. Tan and L. Ng, "Calculation of the equilibrium antiproton spectrum," *Journal of Physics G: Nuclear Physics*, vol. 9, no. 2, p. 227, 1983.

[150] P. Chardonnet, G. Mignola, P. Salati, and R. Taillet, "Galactic diffusion and the antiproton signal of supersymmetric dark matter," *Physics Letters B*, vol. 384, no. 1-4, pp. 161–168, 1996.

[151] D. Maurin, R. Taillet, F. Donato, P. Salati, A. Barrau, and G. Boudoul, "Galactic cosmic ray nuclei as a tool for astroparticle physics," *arXiv preprint astro-ph/0212111*, 2002.

[152] O. Adriani, G. Barbarino, G. Bazilevskaya, R. Bellotti, M. Boezio, E. Bogomolov, L. Bonechi, M. Bongi, V. Bonvicini, S. Bottai, *et al.*, "An anomalous positron abundance in cosmic rays with energies 1.5–100 gev," *Nature*, vol. 458, no. 7238, pp. 607–609, 2009.

[153] J. Liu, Q. Yuan, X.-J. Bi, H. Li, and X. Zhang, "Cosmic ray monte carlo: A global fitting method in studying the properties of the new sources of cosmic e±excesses," *Physical Review D*, vol. 85, no. 4, p. 043507, 2012.

[154] S. Profumo, "Dissecting cosmic-ray electron-positron data with occam's razor: the role of known pulsars," *Open Physics*, vol. 10, no. 1, pp. 1–31, 2012.

[155] K. Cheng, C. Ho, and M. Ruderman, "Energetic radiation from rapidly spinning pulsars. i-outer magnetosphere gaps. ii-vela and crab," *The Astrophysical Journal*, vol. 300, pp. 500–539, 1986.

[156] A. Cheng, M. Ruderman, and P. Sutherland, "Current flow in pulsar magnetospheres," *The Astrophysical Journal*, vol. 203, pp. 209–212, 1976.

[157] M. Rees and J. E. Gunn, "The origin of the magnetic field and relativistic particles in the crab nebula," *Monthly Notices of the Royal Astronomical Society*, vol. 167, no. 1, pp. 1–12, 1974.

[158] P. Slane, "Pulsar wind nebulae," *arXiv preprint arXiv:1703.09311*, 2017.

[159] D. Grasso, S. Profumo, A. Strong, L. Baldini, R. Bellazzini, E. Bloom, J. Bregeon, G. Di Bernardo, D. Gaggero, N. Giglietto, *et al.*, "On possible interpretations of the high energy electron–positron spectrum measured by the fermi large area telescope," *Astroparticle Physics*, vol. 32, no. 2, pp. 140–151, 2009.

[160] D. Hooper, I. Cholis, T. Linden, and K. Fang, "Hawc observations strongly favor pulsar interpretations of the cosmic-ray positron excess," *Physical Review D*, vol. 96, no. 10, p. 103013, 2017.

[161] L. Feng, R.-Z. Yang, H.-N. He, T.-K. Dong, Y.-Z. Fan, and J. Chang, "Ams-02 positron excess: new bounds on dark matter models and hint for primary electron spectrum hardening," *Physics Letters B*, vol. 728, pp. 250–255, 2014.

[162] A. Ibarra, A. S. Lamperstorfer, and J. Silk, "Dark matter annihilations and decays after the ams-02 positron measurements," *Physical Review D*, vol. 89, no. 6, p. 063539, 2014.

[163] M. S. Potgieter, "Solar modulation of cosmic rays," *Living Reviews in Solar Physics*, vol. 10, no. 1, pp. 1–66, 2013.

[164] K. Fang, X.-J. Bi, and P.-F. Yin, "Reanalysis of the pulsar scenario to explain the cosmic positron excess considering the recent developments," *The Astrophysical Journal*, vol. 884, no. 2, p. 124, 2019.

[165] D. Hooper, T. Linden, and P. Mertsch, "What does the pamela antiproton spectrum tell us about dark matter?," *Journal of Cosmology and Astroparticle Physics*, vol. 2015, no. 03, p. 021, 2015.

[166] H.-B. Jin, Y.-L. Wu, and Y.-F. Zhou, "Cosmic ray propagation and dark matter in light of the latest ams-02 data," *Journal of Cosmology and Astroparticle Physics*, vol. 2015, no. 09, p. 049, 2015.

[167] J. Feng, N. Tomassetti, and A. Oliva, "Bayesian analysis of spatial-dependent cosmic-ray propagation: astrophysical background of antiprotons and positrons," *Physical Review D*, vol. 94, no. 12, p. 123007, 2016.

[168] K. Hamaguchi, T. Moroi, and K. Nakayama, "Ams-02 antiprotons from annihilating or decaying dark matter," *Physics Letters B*, vol. 747, pp. 523–528, 2015.

[169] G. Giesen, M. Boudaud, Y. Génolini, V. Poulin, M. Cirelli, P. Salati, and P. D. Serpico, "Ams-02 antiprotons, at last! secondary astrophysical component and immediate implications for dark matter," *Journal of Cosmology and Astroparticle Physics*, vol. 2015, no. 09, p. 023, 2015.

[170] A. Cuoco, M. Krämer, and M. Korsmeier, "Novel dark matter constraints from antiprotons in light of ams-02," *Physical review letters*, vol. 118, no. 19, p. 191102, 2017.

[171] M.-Y. Cui, Q. Yuan, Y.-L. S. Tsai, Y.-Z. Fan, *et al.*, "Possible dark matter annihilation signal in the ams-02 antiproton data," *Physical Review Letters*, vol. 118, no. 19, p. 191101, 2017.

[172] I. Cholis, T. Linden, and D. Hooper, "A robust excess in the cosmic-ray antiproton spectrum: implications for annihilating dark matter," *Physical Review D*, vol. 99, no. 10, p. 103026, 2019.

[173] J. Heisig, M. Korsmeier, and M. W. Winkler, "Dark matter or correlated errors: Systematics of the ams-02 antiproton excess," *Physical Review Research*, vol. 2, no. 4, p. 043017, 2020.

[174] A. Abdo, M. Ackermann, M. Ajello, L. Baldini, J. Ballet, G. Barbiellini, D. Bastieri, K. Bechtol, R. Bellazzini, B. Berenji, *et al.*, "Constraints on cosmological dark matter annihilation from the fermi-lat isotropic diffuse gamma-ray measurement," *Journal of Cosmology and Astroparticle Physics*, vol. 2010, no. 04, p. 014, 2010.

[175] M. Ackermann, A. Albert, B. Anderson, L. Baldini, J. Ballet, G. Barbiellini, D. Bastieri, K. Bechtol, R. Bellazzini, E. Bissaldi, *et al.*, "Dark matter constraints from observations of 25 milky way satellite galaxies with the fermi large area telescope," *Physical Review D*, vol. 89, no. 4, p. 042001, 2014.

[176] L. Goodenough and D. Hooper, "Possible evidence for dark matter annihilation in the inner milky way from the fermi gamma ray space telescope," *arXiv preprint arXiv:0910.2998*, 2009.

[177] K. N. Abazajian and M. Kaplinghat, "Detection of a gamma-ray source in the galactic center consistent with extended emission from dark matter annihilation and concentrated astrophysical emission," *Physical Review D*, vol. 86, no. 8, p. 083511, 2012.

[178] K. N. Abazajian, N. Canac, S. Horiuchi, and M. Kaplinghat, "Astrophysical and dark matter interpretations of extended gamma-ray emission from the galactic center," *Physical Review D*, vol. 90, no. 2, p. 023526, 2014.

[179] T. Daylan, D. P. Finkbeiner, D. Hooper, T. Linden, S. K. Portillo, N. L. Rodd, and T. R. Slatyer, "The characterization of the gamma-ray signal from the central milky way: A case for annihilating dark matter," *Physics of the Dark Universe*, vol. 12, pp. 1–23, 2016.

[180] C. Gordon and O. Macias, "Dark matter and pulsar model constraints from galactic center fermi-lat gamma-ray observations," *Physical Review D*, vol. 88, no. 8, p. 083521, 2013.

[181] A. Boyarsky, D. Malyshev, and O. Ruchayskiy, "A comment on the emission from the galactic center as seen by the fermi telescope," *Physics Letters B*, vol. 705, no. 3, pp. 165–169, 2011.

[182] J. Petrović, P. D. Serpico, and G. Zaharijaš, "Galactic center gamma-ray "excess" from an active past of the galactic centre?," *Journal of Cosmology and Astroparticle Physics*, vol. 2014, no. 10, p. 052, 2014.

[183] K. N. Abazajian, "The consistency of fermi-lat observations of the galactic center with a millisecond pulsar population in the central stellar cluster," *Journal of Cosmology and Astroparticle Physics*, vol. 2011, no. 03, p. 010, 2011.

[184] D. Hooper, I. Cholis, T. Linden, J. M. Siegal-Gaskins, and T. R. Slatyer, "Millisecond pulsars cannot account for the inner galaxy's gev excess," *Physical Review D*, vol. 88, no. 8, p. 083009, 2013.

[185] F. Calore, I. Cholis, and C. Weniger, "Background model systematics for the fermi gev excess," *Journal of Cosmology and Astroparticle Physics*, vol. 2015, no. 03, p. 038, 2015.

[186] M. Di Mauro, "Characteristics of the galactic center excess measured with 11 years of f e r m i-lat data," *Physical Review D*, vol. 103, no. 6, p. 063029, 2021.

[187] G. Steigman, B. Dasgupta, and J. F. Beacom, "Precise relic wimp abundance and its impact on searches for dark matter annihilation," *Physical Review D*, vol. 86, no. 2, p. 023506, 2012.

[188] M. Weber and W. de Boer, "Determination of the local dark matter density in our galaxy," *Astronomy & Astrophysics*, vol. 509, p. A25, 2010.

[189] M. Benito, A. Cuoco, and F. Iocco, "Handling the uncertainties in the galactic dark matter distribution for particle dark matter searches," *Journal of Cosmology and Astroparticle Physics*, vol. 2019, no. 03, p. 033, 2019.

[190] J. Kopp, "Constraints on dark matter annihilation from ams-02 results," *Physical Review D*, vol. 88, no. 7, p. 076013, 2013.

[191] M. S. Longair, *High energy astrophysics*. Cambridge university press, 2010.

[192] S. Colafrancesco, S. Profumo, and P. Ullio, "Multi-frequency analysis of neutralino dark matter annihilations in the coma cluster," *Astronomy & Astrophysics*, vol. 455, no. 1, pp. 21–43, 2006.

[193] A. Tamm, E. Tempel, P. Tenjes, O. Tihhonova, and T. Tuvikene, "Stellar mass map and dark matter distribution in m 31," *Astronomy & Astrophysics*, vol. 546, p. A4, 2012.

[194] Y. Sofue, "Dark halos of m 31 and the milky way," *Publications of the Astronomical Society of Japan*, vol. 67, no. 4, p. 75, 2015.

[195] B. Ruiz-Granados, J. Rubiño-Martín, E. Florido, and E. Battaner, "Magnetic fields and the outer rotation curve of m31," *The Astrophysical Journal Letters*, vol. 723, no. 1, p. L44, 2010.

[196] R. Beck, "The magnetic field in m31," *Astronomy and Astrophysics*, vol. 106, pp. 121–132, 1982.

[197] M. H. Chan, L. Cui, J. Liu, and C. S. Leung, "Ruling out 100–300 gev thermal relic annihilating dark matter by radio observation of the andromeda galaxy," *The Astrophysical Journal*, vol. 872, no. 2, p. 177, 2019.

[198] A. Ficarra, G. Grueff, and G. Tomassetti, "A new bologna sky survey at 408 mhz," *Astronomy and Astrophysics Supplement Series*, vol. 59, pp. 255–347, 1985.

[199] E. L. Łokas and G. A. Mamon, "Dark matter distribution in the coma cluster from galaxy kinematics: breaking the mass–anisotropy degeneracy," *Monthly Notices of the Royal Astronomical Society*, vol. 343, no. 2, pp. 401–412, 2003.

[200] Y. Chen, T. Reiprich, H. Böhringer, Y. Ikebe, and Y.-Y. Zhang, "Statistics of x-ray observables for the cooling-core and non-cooling core galaxy clusters," *Astronomy & Astrophysics*, vol. 466, no. 3, pp. 805–812, 2007.

[201] A. Bonafede, L. Feretti, M. Murgia, F. Govoni, G. Giovannini, D. Dallacasa, K. Dolag, and G. Taylor, "The coma cluster magnetic field from faraday rotation measures," *Astronomy & Astrophysics*, vol. 513, p. A30, 2010.

[202] M. Thierbach, U. Klein, and R. Wielebinski, "The diffuse radio emission from the coma cluster at 2.675 ghz and 4.85 ghz," *Astronomy & Astrophysics*, vol. 397, no. 1, pp. 53–61, 2003.

[203] F. Durret, K.-i. Wakamatsu, T. Nagayama, C. Adami, and A. Biviano, "Ophiuchus: An optical view of a very massive cluster of galaxies

hidden behind the milky way," *Astronomy & Astrophysics*, vol. 583, p. A124, 2015.

[204] G. Beck, "Hunting dark matter in galaxy clusters with non-thermal electrons," *Monthly Notices of the Royal Astronomical Society*, vol. 494, no. 1, pp. 1128–1132, 2020.

[205] M. Murgia, D. Eckert, F. Govoni, C. Ferrari, M. Pandey-Pommier, J. Nevalainen, and S. Paltani, "Gmrt observations of the ophiuchus galaxy cluster," *Astronomy & Astrophysics*, vol. 514, p. A76, 2010.

[206] G. Beck, "An excess of excesses examined via dark matter radio emissions from galaxies," *Journal of Cosmology and Astroparticle Physics*, vol. 2019, no. 08, p. 019, 2019.

[207] M. H. Chan, C. F. Yeung, L. Cui, and C. S. Leung, "Analysing the radio flux density profile of the m31 galaxy: a possible dark matter interpretation," *Monthly Notices of the Royal Astronomical Society*, vol. 501, no. 4, pp. 5692–5696, 2021.

[208] Y. Zhao, X.-J. Bi, H.-Y. Jia, P.-F. Yin, and F.-R. Zhu, "Constraint on the velocity dependent dark matter annihilation cross section from fermi-lat observations of dwarf galaxies," *Physical Review D*, vol. 93, no. 8, p. 083513, 2016.

[209] S. E. Koposov, V. Belokurov, G. Torrealba, and N. W. Evans, "Beasts of the southern wild: Discovery of nine ultra faint satellites in the vicinity of the magellanic clouds," *The Astrophysical Journal*, vol. 805, no. 2, p. 130, 2015.

[210] J. D. Simon, A. Drlica-Wagner, T. Li, B. Nord, M. Geha, K. Bechtol, E. Balbinot, E. Buckley-Geer, H. Lin, J. Marshall, *et al.*, "Stellar kinematics and metallicities in the ultra-faint dwarf galaxy reticulum ii," *The Astrophysical Journal*, vol. 808, no. 1, p. 95, 2015.

[211] S. E. Koposov, A. R. Casey, V. Belokurov, J. R. Lewis, G. Gilmore, C. Worley, A. Hourihane, S. Randich, T. Bensby, A. Bragaglia, *et al.*, "Kinematics and chemistry of recently discovered reticulum 2 and horologium 1 dwarf galaxies," *The Astrophysical Journal*, vol. 811, no. 1, p. 62, 2015.

[212] V. Bonnivard, C. Combet, D. Maurin, A. Geringer-Sameth, S. M. Koushiappas, M. G. Walker, M. Mateo, E. W. Olszewski, and J. I.

Bailey III, "Dark matter annihilation and decay profiles for the reticulum ii dwarf spheroidal galaxy," *The Astrophysical Journal Letters*, vol. 808, no. 2, p. L36, 2015.

[213] A. Albert, B. Anderson, K. Bechtol, A. Drlica-Wagner, M. Meyer, M. Sánchez-Conde, L. Strigari, M. Wood, T. Abbott, F. B. Abdalla, *et al.*, "Searching for dark matter annihilation in recently discovered milky way satellites with fermi-lat," *The Astrophysical Journal*, vol. 834, no. 2, p. 110, 2017.

[214] N. Evans, J. Sanders, and A. Geringer-Sameth, "Simple j-factors and d-factors for indirect dark matter detection," *Physical Review D*, vol. 93, no. 10, p. 103512, 2016.

[215] M. G. Walker, M. Mateo, E. W. Olszewski, J. Penarrubia, N. W. Evans, and G. Gilmore, "A universal mass profile for dwarf spheroidal galaxies?," *arXiv preprint arXiv:0906.0341*, 2009.

[216] J. J. Adams, J. D. Simon, M. H. Fabricius, R. C. van den Bosch, J. C. Barentine, R. Bender, K. Gebhardt, G. J. Hill, J. D. Murphy, R. Swaters, *et al.*, "Dwarf galaxy dark matter density profiles inferred from stellar and gas kinematics," *The Astrophysical Journal*, vol. 789, no. 1, p. 63, 2014.

[217] J. A. Cembranos, Á. de la Cruz-Dombriz, V. Gammaldi, and M. Méndez-Isla, "Ska-phase 1 sensitivity to synchrotron radio emission from multi-tev dark matter candidates," *Physics of the Dark Universe*, vol. 27, p. 100448, 2020.

[218] J. L. Feng, M. Kaplinghat, and H.-B. Yu, "Sommerfeld enhancements for thermal relic dark matter," *physical Review D*, vol. 82, no. 8, p. 083525, 2010.